Supplementary Materials for

A sluggish mid-Proterozoic biosphere and its effect on Earth's redox balance

Supplementary Methods

1. Model description

1.1 General description of the Precambrian CANOPS model

1.1.1 Overview

CANOPS is a 1-D (vertically resolved) intermediate complexity box model of ocean biogeochemistry (see Fig. 1a for the schematic structure) (Ozaki & Tajika, 2013 ; Reinhard et al., 2017 ; Ozaki et al., 2011). It couples a diffusion-advection model of the global ocean with a biogeochemical model and a parameterized sediment model. The ocean circulation model represents a general and robust scheme that is capable of producing well-resolved modern profiles of circulation tracers using realistic parameter values (The model's physical set up can be found elsewhere (Ozaki & Tajika, 2013)), and the coupled biogeochemical model and the parameterized sediment model include explicit representation of a variety of biogeochemical processes, such as biological productivity in the sunlit surface oceans, a series of respiration pathways and secondary redox reactions under oxic and anoxic conditions, and deposition, decomposition and burial of biogenic materials in marine sediments, allowing a mechanistically based examination of the biogeochemical processes.

A new version of the CANOPS model is designed to facilitate simulation for a wide range of biogeochemical conditions so as to permit quantitative examination of the global O_2 budget under the Precambrian conditions. The main improvements are an open-system modelling of marine S cycle (see Section 1.2) and global CH_4 cycle (Fig. 1b,c). Ocean biogeochemical tracers considered are phosphate (PO_4^{3-}), nitrate (NO_3^-), total ammonia (ΣNH_3), dissolved oxygen (O_2), sulphate (SO_4^{2-}), total sulphide (ΣH_2S), and methane (CH_4). The suite of metabolic reactions included in the model is listed in Table S1. Rate constants for these reactions are taken from the literature. The formulations and parameters are listed in Tables S2 and S3.

The model's biogeochemical scheme is based on the cycling of the primary nutrient (phosphate) which limits biological productivity (see Section 1.3). It is assumed that nitrogen required to

sustain productivity is always compensated by the activity of nitrogen fixers. The C-N-P stoichiometry of producers responds dynamically to phosphorus availability in the surface layer (Reinhard et al., 2017). The burial of organic carbon and phosphorus are described by simplified parametric laws based on empirical relationships from modern day observations (Ozaki & Tajika, 2013 ; Ozaki et al., 2011 ; Reinhard et al., 2017). The organic carbon burial flux at each water depth is calculated by the burial efficiency (BE_{oc}), which is defined here as the fraction buried in sediments to that deposited on the ocean floor at each water depth and a function of sedimentation rate and bottom water [O_2] (Reinhard et al., 2017 ; Dale et al., 2012). The organic matter other than burial is subject to decomposition. The benthic denitrification rate is estimated with a polynomial function (Middelburg et al., 1996) (see Section 1.5). The fraction of aerobic degradation in total sedimentary respiration is calculated based on the oxygen exposure time, which is estimated by the oxygen penetration depth (OPD) divided by linear sedimentation rate. OPD is calculated by a simplified parametric law obtained from a 1-D early-diagenetic model of C and O_2 (see Section 1.6). The remaining fraction of remineralized POM is explained by MSR and/or methanogenesis. The redox-dependent phosphorus burial is also taken into account with empirical relationships based on the previous studies (Ozaki & Tajika, 2013 ; Ozaki et al., 2011 ; Reinhard et al., 2017).

The net air-sea gas exchange of O_2, H_2S, NH_3 and CH_4 is quantified according to the stagnant film model (Liss & Slater, 1974 ; Kharecha et al., 2005) (see Section 1.7). We assume that all reduced sulphur gases (SO_2 and H_2S) entering the atmosphere via terrestrial volcanisms is oxidized to sulphate and is carried to the surface ocean. The atmospheric SO_2 and H_2S concentrations are thus set at 0, and H_2S flow past the surface layer of the ocean to the atmosphere is converted to an equal influx of SO_4^{2-} to the surface ocean. If atmospheric O_2 levels are lower than ~1% PAL it can be expected that there are spatial heterogeneity of the gas exchange flux of these gases (Olson et al., 2016); for example primary productivity (and O_2 generation) would be more active at coastal regions than at open-ocean gyre regions. Because CANOPS model resolves only two regions for surface oceans (low-mid latitude region L and high latitude region H), it tends to overestimate the oxidation of reductants in surface mixing layers. To mitigate this model limitation for CH_4 degassing flux, the aerobic oxidation rate of CH_4 is arbitrarily decreased to 1×10^{-7} of the standard value in surface layers. No continental abiotic and thermogenic CH_4 flux is taken into account. The atmospheric CH_4 concentration is explicitly modelled as balances of its source (degassing from the ocean) and sink (photooxidation), where CH_4 photooxidation is calculated according to a parameterized O_2

dependent function proposed by (Goldblatt et al., 2006). The current version of CANOPS model treats atmospheric O_2 levels as one of the boundary conditions because imposing, rather than modeling, atmospheric O_2 not only simplifies the model but significantly reduces computing time. The O_2 budget in the coupled ocean-atmosphere system can be examined in the framework of the global redox budget (see Section 1.8).

1.2 Global sulphur cycle

The original CANOPS model (Ozaki & Tajika, 2013) treated two sulphur species, SO_4^{2-} and ΣH_2S, in a closed cycle: Neither inputs from rivers, hydrothermal vents, and submarine volcanoes, nor outputs due to evaporite formation and sedimentary pyrite burial were simulated. To explore the conditions and dynamics of Proterozoic sulphur cycling, we developed a sulphur cycle modelling approach in which the ocean sulphur balance is explicitly evaluated (Fig. 1b). Sulphur enters the ocean mainly from river runoff, J_S^{riv}, with minor contributions from aerial volcanism, J_S^{vol}, and hydrothermal vents, J_S^{MOR}:

$$J_S^{in} = J_S^{riv} + J_S^{vol} + J_S^{MOR} . \tag{S1}$$

The estimates of modern J_S^{vol} and J_S^{MOR} fall within the range of ~0.2–2 Tmol S yr^{-1} (1 T = 10^{12}) and ~0.1–0.9 Tmol S yr^{-1}, respectively (Kagoshima et al., 2015 ; Catling & Kasting, 2017 ; Raiswell & Canfield, 2012 ; Walker & Brimblecombe, 1985). We adopted a recent estimate (Kagoshima et al., 2015) of 0.7 Tmol S yr^{-1} and 0.1 Tmol S yr^{-1} for these fluxes. Given the uncertainty in the value of J_S^{vol} and J_S^{MOR} during the Proterozoic, the most straight forward assumption is to assume a typical value in the modern settings, even though there are likely differences in the tectonic settings. The present riverine flux J_S^{riv*} is 2.6 Tmol S yr^{-1} (Raiswell & Canfield, 2012), representing the dominant source for the oceans. Riverine flux is written as the sum of the gypsum weathering flux J_{gyp}^{w} and the oxidative weathering of pyrite J_{py}^{w} and depends directly or indirectly on the oxidation state of the atmosphere:

$$J_S^{riv} = J_{gyp}^{w} + J_{py}^{w} . \tag{S2}$$

Based on previous studies (Berner, 2009 ; Wortmann & Paytan, 2012 ; Bergman et al., 2004 ; Markovic et al., 2015), a 3:1 ratio in modern rivers of sulphate from gypsum versus pyrite weathering is assumed. Gypsum weathering flux is assumed to be proportional to its sedimentary reservoir size:

$$J_{gyp}^{w} = f_{erosion} \times \left(\frac{S_{gyp}}{S_{gyp}^{*}} \right) \times J_{gyp}^{w*}, \tag{S3}$$

where $f_{erosion}$ is a factor expressing the effect of continental denudation/erosion on terrestrial weathering, S_{gyp} denotes the sedimentary reservoir size of gypsum and * represents present value. Pyrite weathering is divided to biogenic ($J_{py}^{w\text{-}bio}$) and abiotic ($J_{py}^{w\text{-}abio}$) weathering fluxes:

$$J_{py}^{w} = J_{py}^{w\text{-}abio} + J_{py}^{w\text{-}bio}, \tag{S4}$$

$$J_{py}^{w\text{-}abio} = f_{erosion} f_{O_2} \times \left(\frac{S_{py}}{S_{py}^{*}} \right) \times J_{py}^{w\text{-}abio*}, \tag{S5}$$

$$J_{py}^{w\text{-}bio} = f_{erosion} f_{\varepsilon} \times \left(\frac{S_{py}}{S_{py}^{*}} \right) \times J_{py}^{w\text{-}bio*}, \tag{S6}$$

where f_{O2} represents the oxygen-dependency of abiotic oxidation. We estimate threshold values of atmospheric O_2 level between transport-limited, oxygen-dependent, and reaction-limited regimes by considering how pO_2 affects the dissolution time for cubic pyrite grain (τ), which is estimated by $\rho\, l(2km)^{-1}$ where ρ is a density (= 5 g cm^{-3}), l is an initial side length (= 100 μm), k is a pyrite oxidation rate (Williamson & Rimstidt, 1994), and m is a molecular weight of FeS_2 (= 120 g mol^{-1}). Given the typical soil age of 3000 to 10^5 years (Canfield et al., 2000), almost all pyrite derived from bedrock will be oxidized before reaching the surface when pO_2 >~0.35% PAL (i.e., transport-limited regime; f_{O2} = 1). In contrast, if pO_2 is lower than ~3×10^{-4}% PAL, almost all pyrite reaches surface before dissolution (reaction-limited; f_{O2} = 0). Between these regimes a log-linear interpolation was adopted. We assume ~60% of today's pyrite is being oxidized abiotically (Stueken et al., 2012). f_{ε} represents a factor of biotic preferential weathering of sulphur (f_{ε} = 1 for the present, and f_{ε} = 0.8 for the mid-Proterozoic). Previous estimates of present crustal reservoir sizes of gypsum and pyrite sulphur fall in the range of 77–300×10^{18} mol and 155–300×10^{18} mol (Berner, 2006 ; Bottrell & Newton, 2006 ; Yaroshevsky, 2006 ; Kump, 1989 ; Lasaga, 1989 ; Holser et al., 1989 ; Sleep, 2005 ; Schlesinger & Bernhardt, 2013), respectively. We adopted 200×10^{18} mol and 200×10^{18} mol for S_{gyp}^{*} and S_{py}^{*}. The uncertainty of the riverine sulphur flux during the mid-Proterozoic is evaluated in the Monte-Carlo analysis by examining uncertainties in $f_{erosion}$, S_{gyp}, S_{py}, and pO_2 (see Section 2).

Sulphur is removed from the ocean either via pyrite burial (J_{py}^{bur}) or gypsum deposition (J_{gyp}^{bur}). Although the present marine sulphur cycle is out of balance because of a lack of major gypsum formation, sulphur cycle should be regarded as a steady state on the timescales longer than the residence time of sulphur in the ocean (ca. 20 Myr). According to the mass balance calculation of sulphur isotopes, ~10–45% of the removal flux is accounted for by pyrite burial, and with the

residue through the formation of gypsum/anhydrite for the near-modern oceans (Tostevin et al., 2014). We assume that the rate of gypsum deposition is proportional to the ion product of Ca^{2+} and SO_4^{2-} (Berner, 2004) in the low- to mid-latitude surface layer, and can be defined as follows:

$$J_{\mathrm{gyp}}^{\mathrm{bur}} = J_{\mathrm{gyp}}^{\mathrm{bur}*} \times \frac{[\mathrm{Ca}^{2+}]_l \times [\mathrm{SO}_4^{2-}]_l}{[\mathrm{Ca}^{2+}]^* \times [\mathrm{SO}_4^{2-}]^*} \tag{S7}$$

where l denotes the low- to mid-latitude surface layer. Although it is thought that Ca^{2+} concentration in the Proterozoic oceans was higher than the present value (Jones et al., 2015 ; Hardie, 2003), we assume the present value for all experiments in order to render our arguments conservative: Higher $[Ca^{2+}]$ results in lower $[SO_4^{2-}]$ at steady state, all other parameters being equal. Therefore, for a given range of $[SO_4^{2-}]$ constrained by geologic records, lower biological productivity is required because the rate of microbial sulphate reduction (MSR) controls the pyrite burial rate (see equation (S8) below). $J_{\mathrm{gyp}}^{\mathrm{bur}*}$ is determined by assuming that gypsum deposition accounts for ~60% of the total sulphur removal from the near-modern ocean.

The geological data of sulphur isotopes demonstrates that pyrite burial was a dominant removal pathway for sulphur until the Phanerozoic (Canfield & Farquhar, 2009 ; Canfield, 2004). The rate of pyrite precipitation in sediments would be proportional to the sulphide production rate at the sediment-water interface, j_{H2S} (in mol S m^{-2} yr^{-1}):

$$j_{\mathrm{py}}^{\mathrm{bur}} = e_{\mathrm{py}} \times j_{\mathrm{H_2S}} \tag{S8}$$

where the proportional coefficient, e_{py}, represents the burial efficiency of pyrite. The rate of MSR is a function of the oceanic redox state, $[SO_4^{2-}]$ and the availability of degradable organic matter (see below). In the well-oxygenated modern oceans most of sulphide produced by MSR is reoxidized and only a few per cent of sulphide would be buried as pyrite (Canfield, 1991 ; Lin & Morse, 1991 ; Turchyn & Schrag, 2004 ; Bowles et al., 2014 ; Jørgensen, 1982). This efficient oxidation of sulphide is promoted by animal bioturbation (Berner & Westrich, 1985). In the CANOPS model, a standard value of e_{py} was estimated to be ~0.13 in order to achieve a seawater $[SO_4^{2-}]$ of ~30 mM under the reference condition (mimicking the present ocean), showing a good agreement with the modern observations for total rate of MSR (Berner, 1982 ; Canfield, 1989 ; Raiswell & Canfield, 2012). In contrast, the value of e_{py} during the Proterozoic would have been much greater because of the absence of bioturbation and pervasive anoxic/ferruginous conditions. We assume that e_{py} asymptotes toward unity with decreasing the bottom water $[O_2]$ (Tarhan et al., 2015). Although our approach does not provide a mechanistic description of the complex process of pyrite precipitation, it is nevertheless suitable for our

purposes. Note that syngenetic pyrite formation in the water column is not taken into account in the present study. Hence simulated ΣH_2S concentrations should be regarded as maximum estimates. It is also important to note that ignoring syngenetic pyrite formation maximizes our estimates of biological production (i.e., biospheric O_2 production), because an additional S sink would result in a drawdown of steady state value of marine $[SO_4^{2-}]$, all other things being equal. The model will then tend to retrieve parameter combinations that yield lower rates of MSR to keep $[SO_4^{2-}]$ in a given range. This can be achieved by decreasing the availability of organic matter (i.e., by reducing biological productivity). Total burial rate of pyrite sulphur J_{py}^{bur} is obtained by integrating j_{py}^{bur} for the whole ocean.

1.3 Marine primary production

The model's biogeochemical scheme is based on the cycling of the primary nutrient (phosphate) which limits biological productivity—the new production is related to the availability of phosphorus within the euphotic zone (Maier-Reimer, 1993 ; Yamanaka & Tajika, 1996 ; Shaffer et al., 2008):

$$j_{oc}^{ex} = \alpha h_m \varepsilon [PO_4^{3-}] \frac{[PO_4^{3-}]}{[PO_4^{3-}] + K_P} \tag{S9}$$

where j_{oc}^{ex} represents new/export production of particulate organic carbon (in unit of mol C m^{-2} yr^{-1}), α denotes C/P stoichiometry of producers, h_m is the mixed layer depth, ε denotes the efficiency factor for phosphorus uptake, and K_P denotes the half-saturation constant. The C-N-P stoichiometry of producers responds dynamically to phosphorus availability in the surface layer (Reinhard et al., 2017). The value of ε for low-mid latitude region is assumed to be 1. In contrast, we assume some lower efficiency for high latitude region because biological production tends to be limited by environmental factors other than phosphate availability (e.g., amount of solar radiation, mixed layer depth, sea-ice formation, and iron availability). The hypothetical P removal process via scavenging by reduced iron species was also introduced for the Precambrian anoxic oceans (Reinhard et al., 2017), where P removal is assumed to be proportional to the phosphate upwelling flux to the low-latitude euphotic zone (L) with a proportional coefficient, 'scavenging efficiency', σ_{scav}. Biological production in the surface mixing layers increases in the concentration of dissolved O_2 and reduces the concentrations of dissolved inorganic phosphorus (DIP) and dissolved inorganic nitrogen (DIN) according to the stoichiometric ratio (R1 and R2; Table S1). DIN consumption is partitioned between nitrate and ammonium, assuming that ammonium is preferentially assimilated and that once all available ammonium is assimilated,

remaining nitrogen demand is borne by nitrate. If nitrogen demand is larger than the availability of DIN, it is assumed to be compensated by nitrogen fixers from the atmosphere. In other words, it is assumed that biological nitrogen fixation keeps pace with phosphorus availability, so that phosphorus (not nitrogen) ultimately determines productivity.

Net primary production (NPP) is calculated by assuming the export ratio, f_{ex}:

$$j_{\mathrm{oc}}^{\mathrm{NPP}} = \frac{j_{\mathrm{oc}}^{\mathrm{ex}}}{f_{ex}} \tag{S10}$$

In the modern ocean globally averaged value of f_{ex} is ~0.2 (Laws et al., 2000). We assumed lower value of 0.1 for the mid-Proterozoic runs, given the absence of organisms, such as diatoms, coccolithophorids and radiolaria, which play an important role in the export of organic matter in the modern oceans. The rate of recycling of organic matter in the photic zone is given by

$$j_{\mathrm{recycle}} = j_{\mathrm{oc}}^{\mathrm{NPP}} - j_{\mathrm{oc}}^{\mathrm{ex}} = \frac{1-f_{\mathrm{ex}}}{f_{\mathrm{ex}}}\, j_{\mathrm{oc}}^{\mathbf{ex}} \tag{S11}$$

The respiration pathway of j_{recycle} depends on the availability of terminal electron acceptors (O_2, NO_3^- and SO_4^{2-}; Eqs.(S12)–(S13)). Following exhaustion of these species as terminal electron acceptors, organic matter remineralization occurs by methanogenesis (R7; Table S1). See Methods section for the treatment of organic matter remineralization in the water column.

1.4 Organic matter decomposition

Decomposition of particulate organic matter (POM) is a key process for modelling biogeochemistry in the ocean. In order to represent the decrease in POM lability with time and water depth, we adopted the so-called multi-G models (Westrich & Berner, 1984) that describe the detailed kinetics of organic matter decomposition (Ozaki & Tajika, 2013 ; Ozaki et al., 2011). POM is described using two degradable fractions (G_1 and G_2) and one inert (G_3) fraction using different rate constants k_i (i=1, 2, 3) for each component. The electron acceptor of the respiration reaction changes from dissolved O_2 to other oxidants as O_2 becomes depleted. We parameterized the dependence of decomposition of POM with a Michaelis-Menten type relationship with respect to the terminal electron acceptors:

$$R_{\mathrm{O_2}} = (\sum k_i G_i)\frac{[\mathrm{O_2}]}{K_{\mathrm{O_2}} + [\mathrm{O_2}]} \tag{S12}$$

$$R_{\mathrm{NO_3}} = (\sum k_i G_i)\frac{K'_{\mathrm{O_2}}}{K'_{\mathrm{O_2}} + [\mathrm{O_2}]}\frac{[\mathrm{NO_3^-}]}{K_{\mathrm{NO_3}} + [\mathrm{NO_3^-}]} \tag{S13}$$

$$R_{SO_4} = (\sum k_i G_i) \frac{K'_{O_2}}{K'_{O_2} + [O_2]} \frac{K'_{NO_3}}{K'_{NO_3} + [NO_3^-]} \frac{[SO_4^{2-}]}{K_{MSR} + [SO_4^{2-}]} \quad \text{(S14)}$$

$$R_{CH_4} = (\sum k_i G_i) \frac{K'_{O_2}}{K'_{O_2} + [O_2]} \frac{K'_{NO_3}}{K'_{NO_3} + [NO_3^-]} \frac{K'_{MSR}}{K'_{MSR} + [SO_4^{2-}]} \quad \text{(S15)}$$

$$= 1 - R_{O_2} - R_{NO_3} - R_{SO_4}$$

where K_{O2}, K_{NO3}, and K_{MSR} are Monod constants, and K'_{O2}, K'_{NO3}, K'_{MSR} are inhibition constants. Half saturation constant for MSR (K_{MSR}) determines the degree to which MSR contributes to the total respiration rates. Because estimates of K_{MSR} in natural environments and pure cultures vary over several orders of magnitude (~0.002–3 mM) (Tarpgaard et al., 2011 ; Pallud & Van Cappellen, 2006), we examine the effect of the value of K_{MSR} on the model output with a Monte Carlo analysis (see Section 2).

Total ammonia (ΣNH_3), total sulphide (ΣH_2S), and methane (CH_4), produced during organic matter degradation, are subject to be oxidized to nitrate, sulphate, and carbon dioxide via a set of secondary redox reactions (Table S1). The CANOPS ocean model includes nitrification (R8), total sulphide oxidation by O_2 (R9), aerobic oxidation of CH_4 by O_2 (R10), and anaerobic oxidation of methane (AOM) by SO_4^{2-} (R11). The rates of secondary redox reactions are formulated using bimolecular rate laws, except for AOM (Beal et al., 2011). Rate constants for these reactions are taken from the literature (Beal et al., 2011). Secondary redox reactions were calculated implicitly with an operator splitting scheme (Steefel & MacQuarrie, 1996) so as to maintain numerical stability.

1.5 Sediment diagenesis and burial

CANOPS model has 2×60 sediment segments, and for each segment the rates of organic matter decomposition and burial are calculated by semi-empirical relationships extracted from ocean sediment data and modelling (Ozaki & Tajika, 2013 ; Ozaki et al., 2011 ; Reinhard et al., 2017). Of the deposited particulate organic carbon (POC), only a small fraction (burial efficiency, BE_{oc}) is buried permanently in the geological record, and remaining fraction is decomposed via a series of respiration process.

The degradation of organic matter is coupled to the availability of terminal electron acceptors, such as O_2, NO_3^-, and SO_4^{2-} as in the water column. Middelburg et al. (Middelburg et al., 1996) have performed a series of experiment (n = 2,000) with a 1-D early diagenetic model of C-N-O_2

to parameterize benthic denitrification $j_{\mathrm{denitr}}^{\mathrm{sed}}$ (μmol C cm^{-2} d^{-1}) as a polynomial function with the depositional flux density of organic carbon $j_{\mathrm{oc}}^{\mathrm{dep}}$ (μmol C cm^{-2} d^{-1}), water depth z (m), and bottom water concentrations of dissolved O_2 and nitrate (μM):

$$\log j_{\mathrm{denitr}}^{\mathrm{sed}} = c_0 + c_1 \log j_{\mathrm{oc}}^{\mathrm{dep}} + c_2 \left(\log j_{\mathrm{oc}}^{\mathrm{dep}}\right)^2 + c_3 \log[\mathrm{NO}_3^-]_{\mathrm{bw}} \log[\mathrm{O}_2]_{\mathrm{bw}} + c_4 \log[\mathrm{NO}_3^-]_{\mathrm{bw}} + c_5 \log[\mathrm{O}_2]_{\mathrm{bw}} + c_6 \log z + c_7 \log j_{\mathrm{oc}}^{\mathrm{dep}} \log[\mathrm{O}_2]_{\mathrm{bw}} \quad \text{(S16)}$$

where c_0 = -2.2567, c_1 = -0.1850, c_2 = -0.2210, c_3 = -0.3995, c_4 = 1.2500, c_5 = 0.4721, c_6 = -0.0996, c_7 = 0.4256. This polynomial function was obtained by examining a parameter space spanning 50 m < z < 6,000 m, 10 μM < $[O_2]_{\mathrm{bw}}$ < 350 μM, and 1 μM < $[NO_3^-]_{\mathrm{bw}}$ < 60 μM. $j_{\mathrm{oc}}^{\mathrm{dep}}$ was allowed to vary within 2 orders of magnitude at each water depth (Middelburg et al., 1996). As pointed out by Romaniello and Derry (Romaniello & Derry, 2010), the predicted contribution of denitrification to total decomposition f_{denitr} can sometimes exceed 100% for $[O_2]_{\mathrm{bw}}$ <10 μM. When the fraction of benthic denitrification to total decomposition exceeds 90%, benthic denitrification is limited in order to avoid unphysical values (Ozaki & Tajika, 2013 ; Romaniello & Derry, 2010).

The remaining degradation is modelled via aerobic respiration, sulphate reduction, and methanogenesis. A fraction of aerobic respiration, f_{aerobic}, is given by

$$f_{\mathrm{aerobic}} = \left(1 - f_{\mathrm{denitr}}\right) \times \left(1 - e^{-k \times t_{\mathrm{OET}}}\right) \quad \text{(S17)}$$

where k is an empirical constant and t_{OET} denotes the oxygen exposure time, which is given by

$$t_{\mathrm{OET}} = \frac{\mathrm{OPD}}{SR} \quad \text{(S18)}$$

where OPD is the oxygen penetration depth (cm) and SR denotes a linear sedimentation rate (cm yr^{-1}). In this study we employed a 1-D early diagenetic model of C and O_2 (see below) and performed a series of experiments (n = 5,652) in order to parameterize OPD as a polynomial function with the following variables: sedimentation rate SR (cm yr^{-1}), bottom water O_2 concentration $[O_2]_{\mathrm{bw}}$ (μM), depositional flux of particulate organic carbon $j_{\mathrm{oc}}^{\mathrm{dep}}$ (in unit of mmol C cm^{-2} yr^{-1}) and bottom water temperature T_{bw} (°C). The variables are allowed to vary over a parameter space spanning 10^{-4} cm yr^{-1} < SR < 10^1 cm yr^{-1}, 10^0 μM < $[O_2]_{\mathrm{bw}}$ < 10^3 μM, 10^{-4} mmol C cm^{-2} yr^{-1} < $j_{\mathrm{oc}}^{\mathrm{dep}}$ < 10^1 mmol C cm^{-2} yr^{-1}, and 0 °C < T_{bw} < 30 °C.

$$\log \mathrm{OPD} = a_0 + a_1 \log SR + a_2 \log[\mathrm{O}_2]_{\mathrm{bw}} + a_3 \log j_{\mathrm{oc}}^{\mathrm{dep}} + a_4 (\log SR)^2 + a_5 (\log[\mathrm{O}_2]_{\mathrm{bw}})^2 + a_6 (\log j_{\mathrm{oc}}^{\mathrm{dep}})^2 + a_7 (\log SR)(\log[\mathrm{O}_2]_{\mathrm{bw}}) + a_8 (\log[\mathrm{O}_2]_{\mathrm{bw}})(\log j_{\mathrm{oc}}^{\mathrm{dep}}) + a_9 (\log SR)(\log j_{\mathrm{oc}}^{\mathrm{dep}}) + a_{10} T_{\mathrm{bw}} \quad \text{(S19)}$$

where a_0 = -2.24869, a_1 = 0.110645, a_2 = 1.12569, a_3 = -0.281005, a_4 = 0.014827, a_5 = -0.124721, a_6 = 0.0894604, a_7 = 0.00279531, a_8 = -0.127797, a_9 = 0.0017995, and a_{10} =

0.0085171. This parametric fit provides a rapid means of obtaining OPD from a 1-D early diagenetic model of C and O_2. Note that equation (S19) above is verified for $[O_2]_{bw}$ >1 μM. When bottom water O_2 concentration is lower than 1 μM, OPD is set at zero.

Fractions of microbial sulphate reduction (MSR) and methanogenesis to total decomposition of organic matter in sediment are given by

$$f_{\mathrm{MSR}} = \left(1 - f_{\mathrm{aerobic}} - f_{\mathrm{denitr}}\right) \times \frac{[\mathrm{SO}_4^{2-}]_{\mathrm{bw}}}{[\mathrm{SO}_4^{2-}]_{\mathrm{bw}} + K_{\mathrm{MSR}}} \tag{S20}$$

$$f_{\mathrm{methan}} = 1 - f_{\mathrm{aerobic}} - f_{\mathrm{denitr}} - f_{\mathrm{MSR}} \tag{S21}$$

The production rate of hydrogen sulphide in sediment, j_{H2S} (mol S m^{-2} yr^{-1}), is given by

$$j_{\mathrm{H_2S}} = \frac{1}{2} f_{\mathrm{MSR}} \left(1 - BE_{\mathrm{oc}}\right) j_{\mathrm{oc}}^{\mathrm{dep}} + j_{\mathrm{AOM}} \tag{S22}$$

where $j_{\mathrm{oc}}^{\mathrm{dep}}$ is the depositional flux of POC (in unit of mol C m^{-2} yr^{-1}) and j_{AOM} denotes the production rate of sulphide via AOM:

$$j_{\mathrm{AOM}} = \frac{1}{2} f_{\mathrm{methan}} \left(1 - BE_{\mathrm{oc}}\right) j_{\mathrm{oc}}^{\mathrm{dep}} \frac{[\mathrm{SO}_4^{2-}]_{\mathrm{bw}}}{[\mathrm{SO}_4^{2-}]_{\mathrm{bw}} + K_{\mathrm{MSR}}} \tag{S23}$$

Here we assume that AOM is proportional to the CH_4 production rate with a sulphate-dependent term. The pyrite precipitation rate is calculated by Eq. (S8).

1.6 Early diagenetic model of C and O_2

The simple early diagenetic model of C and O_2 is employed to obtain the parameterization of OPD (Eq. (19)). The 100 cm thick sediment is vertically divided into 50 layers with an uneven grid. The grid size increases from the sediment-water interface (Δz = 0.25 mm) to the maximum simulated sediment depth (Δz = 1.6 cm). The diagenetic model calculates the transport and the biogeochemical transformation processes at each grid point within these sediment columns as well as the sedimentary burial and recycling fluxes at the model boundaries. The one-dimensional mass conservation equation for POC (wt. %) and dissolved O_2 is given by

$$\frac{\partial \mathrm{POC}}{\partial t} = D_{\mathrm{bio}} \frac{\partial^2 \mathrm{POC}}{\partial z^2} - SR \frac{\partial \mathrm{POC}}{\partial z} - k\mathrm{POC} \tag{S24}$$

$$\frac{\partial [\mathrm{O}_2]}{\partial t} = D_{\mathrm{O_2}} \frac{\partial^2 [\mathrm{O}_2]}{\partial z^2} - r_{\mathrm{O_2}} k\mathrm{POC} \left(\frac{\rho(1-\phi)}{1.2\phi} \right) \frac{[\mathrm{O}_2]}{[\mathrm{O}_2] + K_{\mathrm{O_2}}} \tag{S25}$$

where D_{O2} is the diffusion coefficient of O_2, SR is the sediment accumulation rate, k is the rate constant of organic carbon oxidation (= $2.97\times SR^{0.62}$ yr^{-1}), r_{O2} is an O_2/C ratio for aerobic respiration (= 1.4), ρ is a dry bulk density (= 2.6 g cm^{-3}), K_{O2} is a half-saturation constant for O_2 (= 1 μM), and ϕ is porosity (= 0.8), which is assumed to be constant over the entire sediment column for simplicity. Bioturbation is formulated as a diffusive process with a coefficient D_{bio}. The effective diffusion coefficients of O_2 is then given by

$$D_{O_2} = \frac{D_{O_2}^{T=0} \times \left(1 + \nu_{O_2} T_{bw}\right)}{\theta^2} + D_{bio} \tag{S26}$$

where $D_{O2}^{T=0}$ denotes a tracer diffusion coefficient in seawater of 0°C (= 281 cm^2 yr^{-1}), v_{O2} is a coefficient for temperature dependence of molecular diffusion coefficient (= 0.06 °C^{-1}). In situ diffusion coefficient is further corrected for tortuosity θ, which is related to the pore water resistivity and the porosity via the following expressions (Colman & Holland, 2000 ; Tromp et al., 1995 ; Berner, 1980):

$$\theta^2 = \phi F \tag{S27}$$

$$F = \phi^{-m} \tag{S28}$$

where F is the formation factor, defined as the ratio of the bulk sediment resistivity to the interstitial water resistivity, and m is an empirical constant, varying with sediment type. We assumed the average value for unconsolidated muds (m = 2.7) in this work (Tromp et al., 1995). The particle mixing coefficient by bioturbation D_{bio} is formulated as a function of both sediment accumulation rate and bottom water O_2 concentration (Tromp et al., 1995 ; Wallmann, 2003):

$$D_{bio} = 10^{1.63+0.85\log SR} \frac{[O_2]_{bw}}{[O_2]_{bw} + K_{O_2}} \tag{S29}$$

At the bottom of the sediment column, a no-flux condition was applied.

1.7 Atmosphere-ocean gas exchange

To calculate the gas exchange of O_2, H_2S, NH_3, and CH_4 across the air–sea interface, we employed a stagnant film model (Liss & Slater, 1974). The flux of a gas X across the air–sea interface is controlled by the difference in the partial pressure in the atmosphere and in the surface waters, which can be described by the following formula:

$$J_X^{oa} = v_X^{piston}\left([X]_{aq} - [X]_{sat}\right) \tag{S30}$$

where v_X^{piston}, $[X]_{aq}$, and $[X]_{sat}$ denote piston velocity, the dissolved concentration of species X, and the saturation concentration of species X, respectively. For O_2, the saturation concentration is

calculated based on the solubility (Garcia & Gordon, 1992 ; Sarmiento & Gruber, 2006) and partial pressure:

$$[\mathrm{O_2}]_{\mathrm{sat}} = \left(\frac{1000}{22.3916} \times e^{l}\right) \times \frac{p\mathrm{O_2}}{p\mathrm{O_2}^{*}} \tag{S31}$$

where

$$l = A_0 + A_1 T_{\mathrm{s}} + A_2 T_{\mathrm{s}}^{2} + A_3 T_{\mathrm{s}}^{3} + A_4 T_{\mathrm{s}}^{4} + A_5 T_{\mathrm{s}}^{5} + S \times (B_0 + B_1 T_{\mathrm{s}} + B_2 T_{\mathrm{s}}^{2} + B_3 T_{\mathrm{s}}^{3}) + C_0 S^2 \tag{S32}$$

$$T_{\mathrm{s}} = \ln\left(\frac{298.15 - T}{273.15 + T}\right) \tag{S33}$$

with T in °C. The constants are A_0 = 2.00907, A_1 = 3.22014, A_2= 4.0501, A_3= 4.94457, A_4= -0.256847, A_5 = 3.88767, B_0 = -6.24523$\times 10^{-3}$, B_1 = -7.3761×10^{-3}, B_2 = -1.0341×10^{-2}, B_3 = -8.17083×10^{-3}, and C_0 = -4.88682×10^{-7}. The erroneous $A_3 \times T_{\mathrm{s}}^{2}$ term in the original equation (Garcia & Gordon, 1992) was left out (Sarmiento & Gruber, 2006).

For H_2S and NH_3, $[X]_{sat}$ is given by (Kharecha et al., 2005)

$$[X]_{\mathrm{sat}} = K_X^{\mathrm{Henry}}\, pX \tag{S34}$$

where K_X^{Henry}, and pX denote Henry's law coefficient and partial pressure of species X, respectively. The temperature dependence of X's solubility is expressed as:

$$K_X^{\mathrm{Henry}} = K_X^{\mathrm{Henry}\circ} \exp\left[K_X^{T}\left(\frac{1}{T} - \frac{1}{298.15}\right)\right] \tag{S35}$$

where $K_X^{\mathrm{Henry}\circ}$ denotes the Henry's law coefficient of species X at 25°C, and K_X^{T} is the temperature dependence constant.

$[X]_{aq}$ is the dissolved concentration of X. $[H_2S]_{aq}$ and $[NH_3]_{aq}$ can be written as follows:

$$[\mathrm{H_2S}]_{\mathrm{aq}} = \frac{[\Sigma \mathrm{H_2S}]}{1 + K_{\mathrm{H_2S}}^{\mathrm{dis}} / [\mathrm{H^+}]} \tag{S36}$$

$$[\mathrm{NH_3}]_{\mathrm{aq}} = \frac{[\Sigma \mathrm{NH_3}]}{1 + [\mathrm{H^+}] / K_{\mathrm{NH_3}}^{\mathrm{dis}}} \tag{S37}$$

where $[\Sigma H_2S]$ = $[H_2S]$ + $[HS^-]$ and $[\Sigma NH_3]$ = $[NH_4^+]$ + $[NH_3]$. K_{H2S}^{dis} and K_{NH3}^{dis} are the dissociation constant, defined as follows:

$$K_{\mathrm{H_2S}}^{\mathrm{dis}} = \frac{[\mathrm{HS^-}][\mathrm{H^+}]}{[\mathrm{H_2S}]_{\mathrm{aq}}} \tag{S38}$$

$$K_{\mathrm{H_2S}}^{\mathrm{dis}} = \frac{[\mathrm{NH_3}]_{\mathrm{aq}}[\mathrm{H^+}]}{[\mathrm{NH_4^+}]} \tag{S39}$$

Given values of K_{H2S}^{dis}, K_{NH3}^{dis} and pH (Millero et al., 1988 ; Yao & Millero, 1995), $[H_2S]_{aq}$ and $[NH_3]_{aq}$ can be calculated. H_2S and NH_3 flow past the surface layer of the ocean to the atmosphere are converted to an equal influx of SO_4^{2-} and NO_3^- to the surface ocean.

1.8. Global redox budget

CANOPS model is designed to be a part of a more comprehensive global redox budget (GRB) framework (Fig. 5). Here GRB is defined for the combined ocean-atmosphere system. Because we focus on a weakly oxidized ocean-atmosphere system during the Proterozoic, we keep track of GRB in terms of O_2 equivalents. To do so, we define H_2O, CO_2, N_2, H_2SO_4, and FeO as reference oxidation states for H, C, N, S, and Fe. Then, oxidizing power of various species X, ϕ_X, is measured in units scaled to the oxidizing power of an O_2 molecule that is defined as +1 (Table S7). For example, in terms of the GRB, burial of one mole of organic carbon is equivalent to gain of one mole of O_2: $CO_2 + H_2O \rightarrow CH_2O + O_2$ (i.e., $\phi_{CH2O} = -1$). On the timescales longer than the residence time of O_2 in the ocean-atmosphere system, O_2 source fluxes should be balanced by its sink fluxes. When we label the redox effect of the flux of species X by the process i on GRB as Φi(X), the global O_2 budget can be written in terms of O_2 equivalents as

$$\frac{dM_{O_2}}{dt} = \Phi_{source} + \Phi_{sink} = 0 \tag{S40}$$

where M_{O2} denotes the total amount of O_2 in the system and

$$\Phi_{source} = \Phi_{bur}(CH_2O) + \Phi_{bur}(FeS) + \Phi_{esc}(CH_4) \tag{S41}$$

$$\begin{aligned}\Phi_{sink} = \Phi_{w}(CH_2O) + \Phi_{w}(FeS) + \Phi_{bur}(Fe(III)) \\ + \Phi_{volc}(SO_2, H_2S) + \Phi_{MOR}(H_2S) + \Phi_{out}(Red)\end{aligned} \tag{S42}$$

where ‘bur’ and ‘w’ represent burial and oxidative weathering, respectively, and 'esc' is hydrogen escape to space. For example, $\Phi_{bur}(CH_2O) = \phi_{CH2O} \times J_{oc}^{bur}$. $\Phi_{volc}(SO_2, H_2S)$ and $\Phi_{MOR}(H_2S)$ denote the effect of outgassing rates of reduced sulphur species via subaerial and submarine volcanism, respectively. We adopt a previous estimate of 0.7 Tmol S yr^{-1} and 0.1 Tmol S yr^{-1} for those sulphur fluxes (Kagoshima et al., 2015), with assuming modern SO_2:H_2S ratio of ~9:1 for the oxidation state of subaerial volcanic gases. This yields a stoichiometric coefficient of -0.65 (= $\phi_{SO2} \times 0.9 + \phi_{H2S} \times 0.1$). Given estimates of J_{oc}^{bur}, J_{py}^{bur}, J_{py}^{w} and J_{Hesc} derived from MC simulations, their redox coefficients on the GRB, and a parameterization for the rate of oxidative weathering of organic matter J_{oc}^{w} and Fe^{3+} precipitation in terrestrial sediments $J_{Fe(III)}^{bur}$ (see below), we can estimate Φ_{out}(Red), which represents the residual reductant (e.g., H_2, CO, CH_4)

input flux via subaerial/submarine volcanisms and metamorphism and/or the oxidant output (Fe^{3+}) needed to match the global O_2 balance;

$$\Phi_{\mathrm{out}}(\mathrm{Red}) = J_{\mathrm{oc}}^{\mathrm{bur}} + 2J_{\mathrm{py}}^{\mathrm{bur}} + J_{\mathrm{Hesc}} - J_{\mathrm{oc}}^{\mathrm{w}} - 2J_{\mathrm{py}}^{\mathrm{w}} - 0.25J_{\mathrm{Fe(III)}}^{\mathrm{bur}} - 0.65J_{\mathrm{volc}}^{\mathrm{S}} - 2J_{\mathrm{MOR}}^{\mathrm{S}} \quad \text{(S43)}$$

For J_{oc}^{w}, we adopt a previously published $(pO_2)^{0.5}$ dependency on atmospheric O_2 level (Bergman et al., 2004 ; Lasaga & Ohmoto, 2002 ; Daines et al., 2017). J_{oc}^{w} is also assumed to be proportional to the value of $f_{erosion}$;

$$J_{\mathrm{oc}}^{\mathrm{w}} = f_{\mathrm{erosion}} \times (p\mathrm{O}_2(\mathrm{PAL}))^{0.5} \times J_{\mathrm{oc}}^{\mathrm{w}*} \quad \text{(S44)}$$

where J_{oc}^{w*} denotes the present value of 10.5 Tmol C yr^{-1}, derived from a reference run of the CANOPS model (see Supplementary Discussion).

Fe(II)-bearing minerals release Fe(II) during terrestrial weathering. A certain fraction of the released Fe(II) is subsequently oxidized to Fe(III) and retained in sediments. This oxidative weathering of 'FeO' minerals and subsequent Fe(III) retention in sediments represents one of the O_2 sinks (Catling & Kasting, 2017) ($4'\mathrm{FeO}' + \mathrm{O}_2 \rightarrow 2\mathrm{Fe}_2\mathrm{O}_3$), which is given by.

$$J_{\mathrm{Fe(III)}}^{\mathrm{bur}} = f_{\mathrm{erosion}} \times \phi \times J_{\mathrm{Fe(III)}}^{\mathrm{bur}*} \quad \text{(S45)}$$

where $J_{Fe(III)}^{bur*}$ denotes the present value (5 Tmol Fe yr^{-1}) (Holland, 1978 ; Catling & Kasting, 2017) and ϕ denotes the 'retention potential' of Fe(III), defined as the ratio of the iron remained as Fe(III) in sediments to the dissolution rate of Fe(II) minerals. Recent studies (Kanzaki & Murakami, 2016 ; Yokota et al., 2013) have constructed a quantitative relationship between ϕ and atmospheric O_2 levels. We adopted a following parameterization based on (Kanzaki & Murakami, 2016)

$$\phi = c_0 + c_1 \times \log(p\mathrm{O}_2(\mathrm{PAL})) + c_2 \times (\log(p\mathrm{O}_2(\mathrm{PAL})))^2 \quad \text{(S46)}$$

where c_0 = 0.9713, c_1 = -0.1095, and c_2 = -0.0737. ϕ is assumed to be unity for $\log(pO_2(PAL)) >$ -1.15 to avoid unphysical value of >1.

2. Monte Carlo (MC) simulations

To assess the whole uncertainty of the model, we perform Monte Carlo simulations with focusing on eight model parameters (Table 1). Here we describe and discuss the range of model parameters representing uncertainty in their values.

The atmospheric O_2 levels (pO_2) during the mid-Proterozoic have been estimated based on a series of geochemical records but are still poorly constrained and the subjects of intense debate (Planavsky et al., 2016 ; Zhang et al., 2016 ; Lyons et al., 2014 ; Planavsky et al., 2014 ; Lenton & Daines, 2017). The absence of a mass-independent fractionation (MIF) of sulphur isotopes from sedimentary rocks after the Great Oxidation Event of 2.4–2.31 Ga (Bekker et al., 2004 ; Farquhar et al., 2000) leads to the accepted views that pO_2 was larger than 0.001% PAL (Pavlov & Kasting, 2002). The absence of detrital uraninite and pyrite in sedimentary records (Holland, 2006 ; Holland, 1984) and Fe concentration in paleosols (Rye & Holland, 1998) have been interpreted as indicating a lower bound of >~1% PAL, with a large uncertainty in the model parameters (Planavsky et al., 2014 ; Kanzaki & Murakami, 2016). The recent modelling studies of paleosol Fe oxidation state (Kanzaki & Murakami, 2016 ; Yokota et al., 2013) indicates a lower estimate of $>10^{-3.9}$–$10^{-1.3}$ PAL for 1.85 Ga Flin Flon paleosol. On the other hand, recent geochemical data, including the absence of oxidative weathering of Cr (Planavsky et al., 2014 ; Cole et al., 2016), the iodine-calcium ratios in carbonates (Hardisty et al., 2017) and REE + Y (Rare Earth Element and yttrium) signatures in the sedimentary rocks (Tang et al., 2016), poses an upper limit of <0.1–1% PAL. It is also important to note that due to the scarcity and fundamental unavailability of geologic records, we cannot rule out the possibility that pO_2 has seen large variations over the course of the Proterozoic (Planavsky et al., 2014). Despite of this large uncertainty in geological constraints, we draw pO_2 from a log-uniform distribution of values between 0.01% and 1% PAL in the standard ('Low O_2') analysis. The lower bound is determined based on the lower estimate of $>10^{-3.9}$ PAL for the Flin Flon paleosol (Kanzaki & Murakami, 2016). This is also sufficiently high for preserving mass-dependent isotope fractionation in sulphur compounds. In the 'Low O_2' scenario we focus on the possibility of pO_2 <1% PAL on the basis of recent geochemical data (Cole et al., 2016 ; Hardisty et al., 2017 ; Planavsky et al., 2014 ; Tang et al., 2016). The possible effect of higher pO_2 levels on our main conclusions is also examined by performing an additional MC analysis with the upper bound of 10% PAL (see 'High O_2' scenario in Table 1), and find a relatively minor effect on the model

results (Fig. 2 and Table S6); the median value of J_{oc}^{bur} and total O_2 production rate are $1.64_{-0.98}^{+1.52}$ Tmol C yr^{-1} and $4.07_{-1.40}^{+1.91}$ Tmol yr^{-1}.

The half saturation constant for MSR, K_{MSR}, plays a critical role in marine sulphur budget because it determines the degree to which the organic matter is decomposed by the MSR for a given SO_4^{2-} concentration. The modern marine sediments are characterized by the MSR community which has high apparent K_{MSR} values (0.1–2.7 mM) (Tarpgaard et al., 2011 ; Pallud & Van Cappellen, 2006), while recent analysis (Tarpgaard et al., 2011) suggests that there are sulphate reducers which are characterized by the micro-molar level K_{MSR} in the modern marine sediments (Tarpgaard et al., 2011). In contrast, the MSR community in the lacustrine sediments is generally characterized by the high sulphate affinity; those apparent K_{MSR} values are estimated to be on the order of 0.01–0.07 mM (Tarpgaard et al., 2011 ; Pallud & Van Cappellen, 2006). In the MC simulations, K_{MSR} is allowed to vary from 0.002 to 2 mM with a log-uniform distribution of probability, bracketing the modern observational range for marine and freshwater sediments. This reflects the large uncertainty in the value of K_{MSR} for the mid-Proterozoic oceans where the composition of microbial communities may vary widely from one region to another. We note, however, that under the mid-Proterozoic conditions ($[SO_4^{2-}]$ <~1 mM) (Luo et al., 2015 ; Lyons & Gill, 2010 ; Planavsky et al., 2012 ; Scott et al., 2014), the activity of sulphate reducers having milli-molar level affinity is likely to be suppressed, and sulphate reducers of high sulphate affinity would have an advantage. Therefore the higher value of K_{MSR} seems less likely for the mid-Proterozoic conditions. In our 'Low O_2' and 'Relaxed' scenario we thus choose 0.5 mM and 1 mM as its upper bounds to examine the uncertainty of K_{MSR} on our conclusions (see also Fig. S4).

An estimate of marine phosphate reservoir size is essential to unravel basic aspects of biological and geochemical evolution, because it is the dominant factors for limiting the productivity of the surface ocean but is poorly constrained for the Proterozoic oceans. The phosphate reservoir size is controlled by the dynamic balance between input mainly via rivers and burial in marine sediments. To account for the effects of the marine phosphorus reservoir size, we vary the value of riverine input rate of reactive phosphorus (R_P) from 0 to 200% of the modern value and the phosphorus 'scavenging efficiency (σ_{scav})' from 0 to 1. Here, σ_{scav} is a proportional coefficient of a hypothetical P scavenging flux by reduced iron species in the anoxic water column (Reinhard

et al., 2017), which is assumed to be proportional to the upward flux of phosphate to the euphotic zone in the low-mid latitude region. It is important to note that even when we ignore this hypothetical P scavenging process, the model merely selects the lower R_P values (<~15% of the present) in order to match the required SO_4^{2-} concentration. In any case, because the oceanic phosphorus inventory is a master parameter controlling the overall productivity and the biogeochemical fluxes in the CANOPS model, our main conclusion would not be changed. Further mechanistic understanding of P sources and sinks is needed to constrain the marine phosphorus residence time.

We draw total crustal reservoir size of sulphur from a Gaussian distribution with a peak at 400×10^{18} mole and a standard deviation of 100×10^{18} mole. This is about mean value of previous estimates of $230–600\times10^{18}$ mole for the present/Phanerozoic value (Berner, 2006 ; Bottrell & Newton, 2006 ; Holser et al., 1989 ; Kump, 1989 ; Lasaga, 1989 ; Schlesinger & Bernhardt, 2013 ; Sleep, 2005 ; Yaroshevsky, 2006). The rarity of Precambrian gypsum deposits and mass balance calculation based on the sulphur isotopic data suggest that oceanic SO_4^{2-} concentration of Proterozoic oceans was substantially low and that gypsum deposition was not a major sulphur removal pathway from the oceans until the Phanerozoic (Canfield & Farquhar, 2009 ; Canfield, 2004). We assume that crustal gypsum reservoir size was relatively minor to that of pyrite sulphur and draw the crustal reservoir size of gypsum (S_{gyp}) from a Gaussian distribution with a peak at 50×10^{18} mole and a standard deviation of 25×10^{18} mole. We think this is a reasonable assumption. The large uncertainty often gives the unrealistic result that S_{gyp} could be negative. We exclude such unreasonable parameter choices by setting S_{gyp} to zero. The crustal reservoir size of pyrite (S_{py}) is calculated by subtracting S_{gyp} from the total crustal reservoir size.

We draw the sinking velocity of POM (V_{POM}) from 0–100 m d^{-1} with a uniform distribution, reflecting the large uncertainty in the efficiency at which organic matter is transferred to abyssal ocean. The range is determined based on the inference that the sinking velocity of organic matter in Precambrian oceans has been slower than that of the Phanerozoic oceans because of the absence of animals and planktons which have dense shells, although the nature of biological pump remains uncertain.

The rates of continental erosion and sediment accumulation in marine environments are closely tied each other, and the effect is expressed by a single parameter, $f_{erosion}$, in this study. This parameter is critical because the oxidative weathering and burial of organic matter and pyrite are controlled by this (Terrestrial weathering and sedimentation rate are scaled by $f_{erosion}$). We assume that the oxidative weathering rate scales in a linear fashion with $f_{erosion}$ (Eq. (S44)). The sediment accumulation rate (*SR*) at the seafloor plays a role in the biogeochemical cycles by affecting the burial efficiencies of carbon and phosphorus and O_2 penetration depth of marine sediment. *SR* is assumed to be proportional to the value of $f_{erosion}$. Its parameter range is set at 0 to 1 with the top end of that range scaled to the present value. This choice is based on the inference that the global erosion/sedimentation rate during the Proterozoic has been lower than that of the near-modern setting. The pronounced cooling during the Pliocene-Pleistocene epoch has induced an increase in erosion rates, especially in glaciated mountain regions, since about 6 Ma by nearly a factor of 2 (Herman et al., 2013). The global accumulation rate of sediments at the modern seafloor is estimated to be ca. $(18–20)\times10^{15}$ g yr^{-1} (Berner, 1982 ; Wallmann et al., 2012 ; Baturin, 2007). In contrast, Garrels and Mackenzie (Garrels, 1971) estimate the average global erosion rate over the Phanerozoic at 6.1×10^{15} g yr^{-1}. Given that the mid-Proterozoic eon (the Nuna supercontinent cycle) has been tectonically quiescent (a stable continental configuration) (Cawood & Hawkesworth, 2014), it seems likely that the value of $f_{erosion}$ would be comparable to the Phanerozoic average, or possibly much lower (Husson & Peters, 2017). We thus set the upper bound at 0.5 in our 'Low O_2' and 'High O_2' scenarios.

In the MC simulations, we sample only simulations that predict a reasonable seawater $[SO_4^{2-}]$ of 0.1–1 mM (Kah et al., 2004 ; Luo et al., 2015 ; Lyons & Gill, 2010 ; Planavsky et al., 2012 ; Scott et al., 2014). The upper bound could be higher, but we note that in that case the model merely retrieve model parameters that predict lower biological productivity (and lower O_2 production rate), strengthening our arguments. This is because MSR (and subsequent pyrite precipitation) should be suppressed in order to achieve higher $[SO_4^{2-}]$. This is achieved by decreasing the availability of organic matter for MSR.

Supplementary Discussion:

1. Standard run

A steady-state simulation for a present-day condition is run to evaluate the overall performance of the new version of CANOPS model against modern oceanographic observations. Parameter values are listed in Table S3. Since the central aim of the present paper is to provide a general examination of ocean biogeochemical cycles in mid-Proterozoic oceans, the calibration effort is restricted to a minimum. Here we provide a brief discussion on globally-integrated biogeochemical flux estimates (Table S4).

Model-generated global fluxes and inventories compare well to independent estimates of C, P, N and S cycles (Table S4). Marine phosphate reservoir size is estimated at 2.7×10^{15} mol, which is consistent with the previous estimate of about 3×10^{15} mol (Delaney, 1998 ; Guidry et al., 2000). Global ocean new production is 8.92 Gt C yr^{-1}. This is also consistent with previously estimated global values of 8.5–12 Gt C yr^{-1} (Dunne et al., 2007 ; Laws et al., 2000 ; Sarmiento & Gruber, 2006 ; Heinze et al., 2009). Of total exported particulate organic matter, 90.6% is decomposed in the water column and the rest (0.84 Gt C yr^{-1}) settles on the sediment surface. The depositional flux of organic carbon in the marginal sediments (<2,000 m) and deep sea sediments (>2,000 m) are estimated at 0.57 Gt C yr^{-1} and 0.26 Gt C yr^{-1}, respectively. These estimates are slightly lower than previous estimates of 0.62–1.98 Gt C yr^{-1} and 0.31–0.62 Gt C yr^{-1} (Bohlen et al., 2012 ; Dunne et al., 2007 ; Muller-Karger et al., 2005 ; Burdige, 2007), respectively. Global average burial efficiency of organic carbon is estimated at 17%, resulting in total burial rate of 0.143 Gt C yr^{-1}, or 12 Tmol C yr^{-1} that is within the range of previous estimates (Berner, 1982 ; Burdige, 2005 ; Muller-Karger et al., 2005).

In the CANOPS model, phosphorus regeneration rate is calculated at each sediment segment based on the depositional flux density j_P^{dep} (= j_{oc}^{dep}/α where j_{oc}^{dep} denotes the depositional flux of organic carbon in units of mol C m^{-2} yr^{-1}) and burial efficiency (BE_P) which is a function of both bottom water O_2 and sedimentation rate (Reinhard et al., 2017). A part of DIP released via respiration to the pore water in marine sediments is redistributed to other burial pools such as iron-hydroxide or carbonate fluorapatite (CFA) within the sediments, but the rest escapes to overlying bottom waters. In the CANOPS model (Ozaki & Tajika, 2013 ; Ozaki et al., 2011 ; Reinhard et al., 2017), three different P pools are considered (organic-P (P_{org}), authigenic-P (P_{auth}), and Fe-hydroxide-bounded-P (P_{Fe})) and the sum of these pools is defined as biologically

reactive P (P_{reac}). In the modern ocean, P burial other than P_{org} is important for total P sink (Ruttenberg, 1993 ; Ruttenberg, 2003 ; Compton et al., 2000), giving rise to the ratio of total organic carbon burial to total P_{react} rate of 65±25 (Algeo & Ingall, 2007). The modelled global average C_{org}/P_{react} ratio of buried sediment is 66.4, consistent with this. The P burial fluxes of P_{org}, P_{auth} and P_{Fe} are estimated at 0.047 Tmol P yr^{-1}, 0.094 Tmol P yr^{-1}, and 0.039 Tmol P yr^{-1}, respectively. Simulated global benthic flux of phosphate is 0.48 Tmol P yr^{-1}, within the range of previous estimates of 0.05–1.25 Tmol P yr^{-1} (Wallmann, 2003 ; Wallmann, 2010 ; Compton et al., 2000 ; Colman & Holland, 2000).

Simulated nitrogen fixation rate is 136 Tg N yr^{-1}, which is within the range of previous estimates of 110–150 Tg N yr^{-1} (Luo et al., 2012 ; Gruber & Sarmiento, 1997 ; Galloway et al., 2004 ; Karl et al., 2002 ; Fowler et al., 2013 ; Duce et al., 2008 ; Deutsch et al., 2007), while a recent study (Großkopf et al., 2012) suggests a higher value of ~180 Tg N yr^{-1}. Simulated denitrification in the water column is 100 Tg N yr^{-1}, within the range of the observational estimates (50–150 Tg N yr^{-1}) (DeVries et al., 2012 ; DeVries et al., 2013 ; Brandes & Devol, 2002 ; Gruber, 2008 ; Gruber & Sarmiento, 2002 ; Oschlies et al., 2008). Modelled benthic denitrification is 61 Tg N yr^{-1}, which is lower than the estimated range of 90–300 Tg N yr^{-1} (DeVries et al., 2012 ; DeVries et al., 2013 ; Brandes & Devol, 2002 ; Eugster & Gruber, 2012 ; Devol, 2015) by a factor of 1.5–5, suggesting that further efforts are required to improve this. Sarmiento and Gruber (Gruber & Sarmiento, 2002) estimate preindustrial value of total source of fixed nitrogen to the ocean at 188±44 Tg N yr^{-1}. Our estimate of 177 Tg N yr^{-1} is in good agreement with this.

Microbial sulphate reduction is a globally important redox process in modern marine sediments. CANOPS model estimates global rate of benthic sulphate reduction at 10.1 Tmol S yr^{-1}. This is considerably lower than previously reported value of gross MSR (40–75 Tmol S yr^{-1}; (Canfield & Farquhar, 2009 ; Jørgensen & Kasten, 2006)) but agree better with net MSR (Bowles et al., 2014). Bowles et al. (Bowles et al., 2014) have estimated global net MSR at 6.2 Tmol S yr^{-1} and 11.3 Tmol S yr^{-1} for z > 200 m depth and z > 0 m depth, respectively. Our estimate is in the range of this. MSR is most pronounced in the shelf, where high fluxes of organic matter to the seafloor lead to small OPD and high production of sulphide, and consequently high precipitation of pyrite. In the CANOPS model, pyrite burial efficiency e_{py} (such as a ratio of pyrite sulphur precipitated to that hydrogen sulphide generated via MSR and AOM) for the sediment

underlying oxic bottom water is determined so that the simulated seawater SO_4^{2-} concentration of the reference run is consistent with modern value of ~30 mM. The tuned value of 0.13 agrees well with observations suggesting that pyrite precipitation rate is about 10–20% of the rate of MSR for sediment accumulation rate of >10^{-2} g cm^{-2} yr^{-1} (Berner & Canfield, 1989 ; Canfield, 1989 ; Raiswell & Canfield, 2012). Our reference value is also consistent with other previous estimates of 0.11–0.2 (Bottrell & Newton, 2006 ; Tarhan et al., 2015 ; Turchyn & Schrag, 2006).

In sum, we conclude that the CANOPS model's performance is sufficient to describe basic global ocean biogeochemical characteristics.

2. Global O_2 balance of the reference state

Global redox (or O_2) balance (GRB) is given by

$$\Phi_{\text{source}} + \Phi_{\text{sink}} = 0 \tag{S47}$$

where Φ_{source} denotes total source flux of O_2 via burial of organic carbon ($J_{\text{oc}}^{\text{bur}}$) and pyrite sulphur ($J_{\text{py}}^{\text{bur}}$) and hydrogen escape to space (J_{Hesc}):

$$\begin{aligned}\Phi_{\text{source}} &= \Phi_{\text{bur}}(\text{CH}_2\text{O}) + \Phi_{\text{bur}}(\text{FeS}) + \Phi_{\text{esc}}(\text{CH}_4) \\ &= J_{\text{oc}}^{\text{bur}} + 2J_{\text{py}}^{\text{bur}} + J_{\text{Hesc}}\end{aligned} \tag{S48}$$

Coefficients are the oxidizing power measured in units of O_2 equivalents (Table S7). Φ_{sink} denotes total O_2 sink flux via oxidative weathering of organic carbon (J_{oc}^{w}) and pyrite sulphur (J_{py}^{w}), Fe^{2+}-bearing mineral oxidation and subsequent Fe^{3+} burial on continent ($J_{\text{Fe(III)}}^{\text{bur}}$), and volcanic input of reduced sulphur ($J_{\text{volc}}^{\text{S}}$) and other gases, such as CO, H_2 and CH_4 (Φ_{out}(Red)):

$$\begin{aligned}\Phi_{\text{sink}} &= \Phi_{\text{w}}(\text{CH}_2\text{O}) + \Phi_{\text{w}}(\text{FeS}) + \Phi_{\text{bur}}(\text{Fe(III)}) \\ &\quad + \Phi_{\text{volc}}(\text{SO}_2, \text{H}_2\text{S}) + \Phi_{\text{MOR}}(\text{H}_2\text{S}) + \Phi_{\text{out}}(\text{Red}) \\ &= -J_{\text{oc}}^{\text{w}} - 2J_{\text{py}}^{\text{w}} - 0.25J_{\text{Fe(III)}}^{\text{bur}} - 0.65J_{\text{volc}}^{\text{S}} - 2J_{\text{MOR}}^{\text{S}} + \Phi_{\text{out}}(\text{Red})\end{aligned} \tag{S49}$$

where

$$\Phi_{\text{out}}(\text{Red}) = -0.5J_{\text{volc}}^{\text{H}_2} - 0.5J_{\text{volc}}^{\text{CO}} - 2J_{\text{abio}}^{\text{CH}_4} \tag{S50}$$

Total outgassing flux of H_2 via subaerial/submarine volcanisms is estimated at 1.4 Tmol yr^{-1}, or 0.7 Tmol O_2 equivalents yr^{-1} (Catling & Kasting, 2017) (Table 2). Surface volcanic flux of CO is about 0.1 Tmol yr^{-1}, or 0.05 Tmol O_2 equivalents yr^{-1} (Catling & Kasting, 2017). The source of abiotic CH_4 from continental hydrothermal systems has been estimated as up to 0.3 Tmol yr^{-1}, or 0.6 Tmol O_2 equivalents yr^{-1} (Fiebig et al., 2009).

At steady state GRB should be achieved. For our reference condition, we can obtain the reference value of oxidative weathering rate of organic carbon (J_{oc}^{w*}), as follows:

$$\begin{aligned} J_{oc}^{w*} &= J_{oc}^{bur*} + 2J_{py}^{bur*} + J_{Hesc}^{*} \\ &\quad - 2J_{py}^{w*} - 0.25J_{Fe(III)}^{bur*} - 0.65J_{volc}^{S*} - 2J_{MOR}^{S*} - 0.5J_{volc}^{H_2*} - 0.5J_{volc}^{CO*} - 2J_{abio}^{CH_4} \end{aligned} \quad \text{(S51)}$$

Given flux values on the right-hand side, J_{oc}^{w*} is estimated as 10.0–10.6 Tmol C yr^{-1}, where the uncertainty is originating from the uncertainty of CH_4 flux from continental hydrothermal systems. We adopt 10.5 Tmol C yr^{-1} as a reference value for the GRB analysis.

3. Sensitivity analysis

3.1. Sensitivity to the range of model parameters

Here we briefly discuss the sensitivity of our results to the model parameters to make our argument clearer. Scatter plots between the control parameters and J_{oc}^{bur} and J_{py}^{bur} illustrates the sensitivity of the model to a few key parameters, as well as its relative insensitivity to several other parameters (Figs S2 and S3). For example, Fig. S2b demonstrates the strong dependency of burial rate of organic carbon (J_{oc}^{bur}) to the value of K_{MSR}; J_{oc}^{bur} larger than the Holocene value would be feasible only when K_{MSR} is comparable or higher than the value observed in the modern marine sediments. The range of this parameter was determined so that it can cover the whole range of observational data over the modern marine and freshwater sediments (see above). However, given the low sulphate levels in the mid-Proterozoic oceans, K_{MSR} value larger than the modern marine sediments seems unlikely. The dependency of J_{oc}^{bur} on the upper bound of K_{MSR} is also shown in Fig. S4a,c. As the maximum value decreases from 2 mM to 0.2 mM, the median value of J_{oc}^{bur} decreases from 2.73 Tmol C yr^{-1} to 1.72 Tmol C yr^{-1}, with a marked decrease in the possibility of high (>6 Tmol C yr^{-1}) value of J_{oc}^{bur}.

Scatter plots also suggest that the global erosion/sedimentation rate exerts a first-order control on J_{oc}^{bur} and J_{py}^{bur} (Figs S2 and S3). The global erosion/sedimentation rate is important, because the high burial rates in the modern and near-modern oceans are thought to be attributed, at least partly, to the high sedimentation rate in the ocean driven by the continental erosion accelerated by the active mountain uplift (e.g., the Himalayas and the Tibetan Plateau), and glacial-interglacial cycles, and human activities. However, it seems likely that the global

erosion/sedimentation rate during the Precambrian has been substantially lower than that of the near-modern setting. Recent geological data of bedrock thermal history reveals that the global erosion rate at present has increased by a factor of 2 due to the enhanced cooling and the waxing and waning of mountain glaciers (Herman et al., 2013). Actually, the previous estimates (Baturin, 2007 ; Berner, 1982) of modern global sedimentation rate far exceed the average value over the Phanerozoic (Garrels, 1971). Given the lack of glacial records during the mid-Proterozoic, it seems likely that the global erosion rate has been lower than the present value by a factor of 2. Fig. S4b,d shows the dependency of J_{oc}^{bur} on the maximum K_{MSR} value with assuming $f_{erosion}$ <0.5, indicating that J_{oc}^{bur} is downwardly revised as the upper bound of $f_{erosion}$ decreases.

4. Carbon isotope model

The mass balance equation for carbon in the atmosphere-ocean system is

$$J_{\text{mantle}} + J_{\text{oc}}^{\text{w}} + J_{\text{carb}}^{\text{w}} = J_{\text{oc}}^{\text{bur}} + J_{\text{carb}}^{\text{bur}} \tag{S52}$$

where J_{mantle} is the total input of carbon from the mantle via outgassing, J_{oc}^{w} is the carbon flux from an oxidative weathering and metamorphism of organic carbon, J_{carb}^{w} is the carbon flux from weathering and metamorphism of carbonates, J_{oc}^{bur} is the burial rate of organic carbon and J_{carb}^{bur} is the carbonate deposition. The associated carbon isotope balance can be represented as

$$\delta_{\text{mantle}} J_{\text{mantle}} + \delta_{\text{oc}} J_{\text{oc}}^{\text{w}} + \delta_{\text{carb}} J_{\text{carb}}^{\text{w}} = (\delta - \Delta) J_{\text{oc}}^{\text{bur}} + \delta J_{\text{carb}}^{\text{bur}} \tag{S53}$$

where δ_{mantle} is the average carbon isotopic composition of the degassing from the mantle, δ_{oc} is the average isotopic composition of the sedimentary organic carbon, δ_{carb} is the average isotopic composition of the crustal carbonate, δ is the average isotopic composition of DIC in the seawater, and Δ denotes the isotopic fractionation between the organic matter and DIC. After substitution and rearrangement of the above equations, we arrive at a generalized equation for f_{org}, the organic fraction of the total organic carbon burial flux:

$$f_{\text{org}} = \frac{\delta - \delta_{\text{in}}}{\Delta} \tag{S54}$$

where δ_{in} denotes the average isotopic composition of input (the outgassing from the mantle plus weathering):

$$\delta_{\text{in}} = \frac{\delta_{\text{mantle}} J_{\text{mantle}} + \delta_{\text{oc}}^{\text{w}} J_{\text{oc}}^{\text{w}} + \delta_{\text{carb}}^{w} J_{\text{carb}}^{w}}{J_{\text{mantle}} + J_{\text{oc}}^{\text{w}} + J_{\text{carb}}^{\text{w}}} . \tag{S55}$$

By using the reference values (Table S8), the modern value of f_{org} is estimated at 0.2 (e.g., (Kump & Arthur, 1999)).

Supplementary Figures

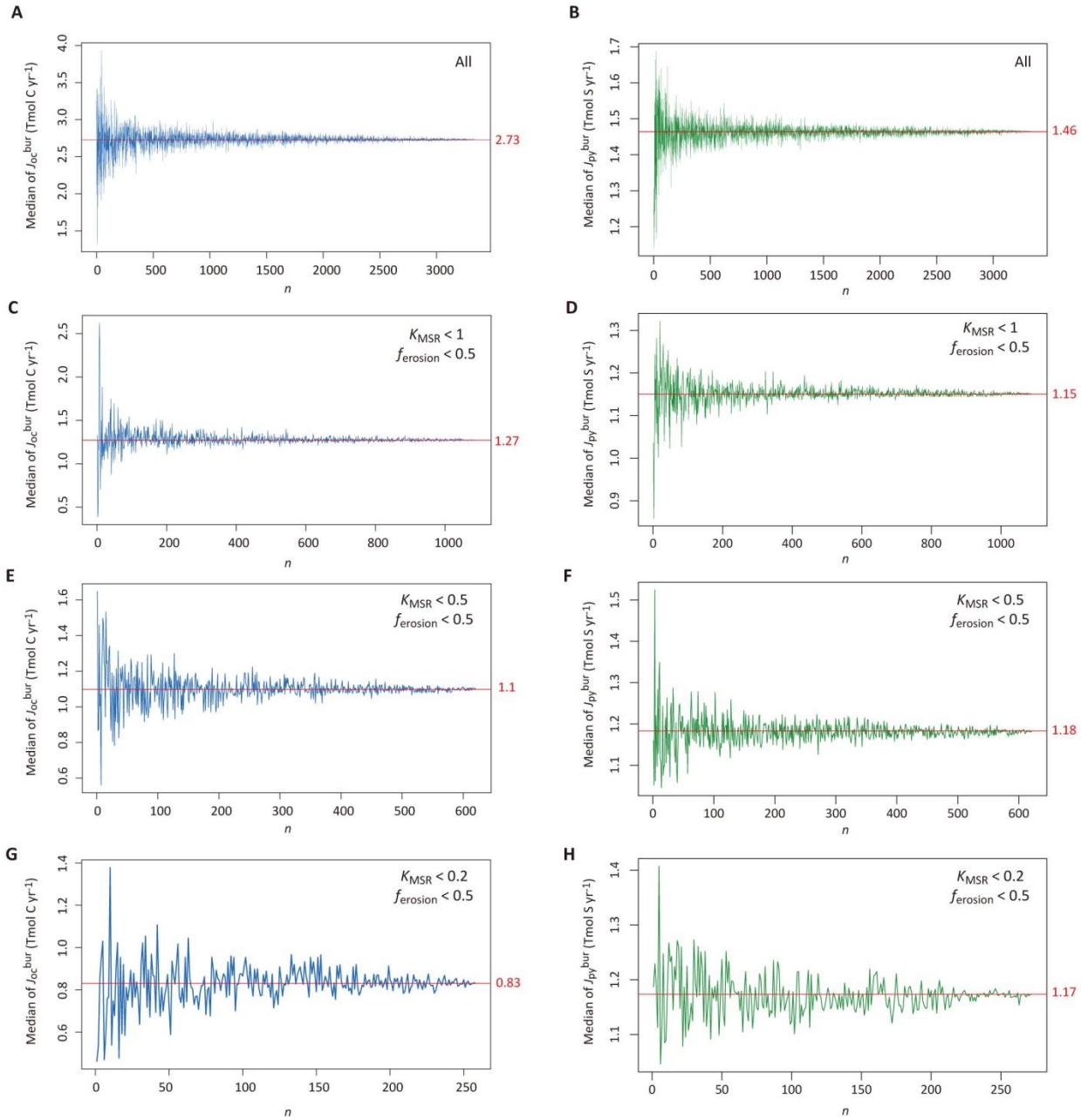

Fig. S1. The median values of J_{oc}^{bur} (left) and J_{py}^{bur} (right) as a function of the number of data. (a, b) Our 'All scenario (see Table S5) (n = 3,342). (c, d) Upper limits for K_{MSR} and $f_{erosion}$ are set at 1 and 0.5, respectively (n = 1,089). (e, f) Our 'standard' scenario (n = 621). Upper limits for K_{MSR} and $f_{erosion}$ are set at 0.5 and 0.5, respectively. (g, h) Upper limits for K_{MSR} and $f_{erosion}$ are set at 0.2 and 0.5, respectively (n = 258). Horizontal red lines denote the median value.

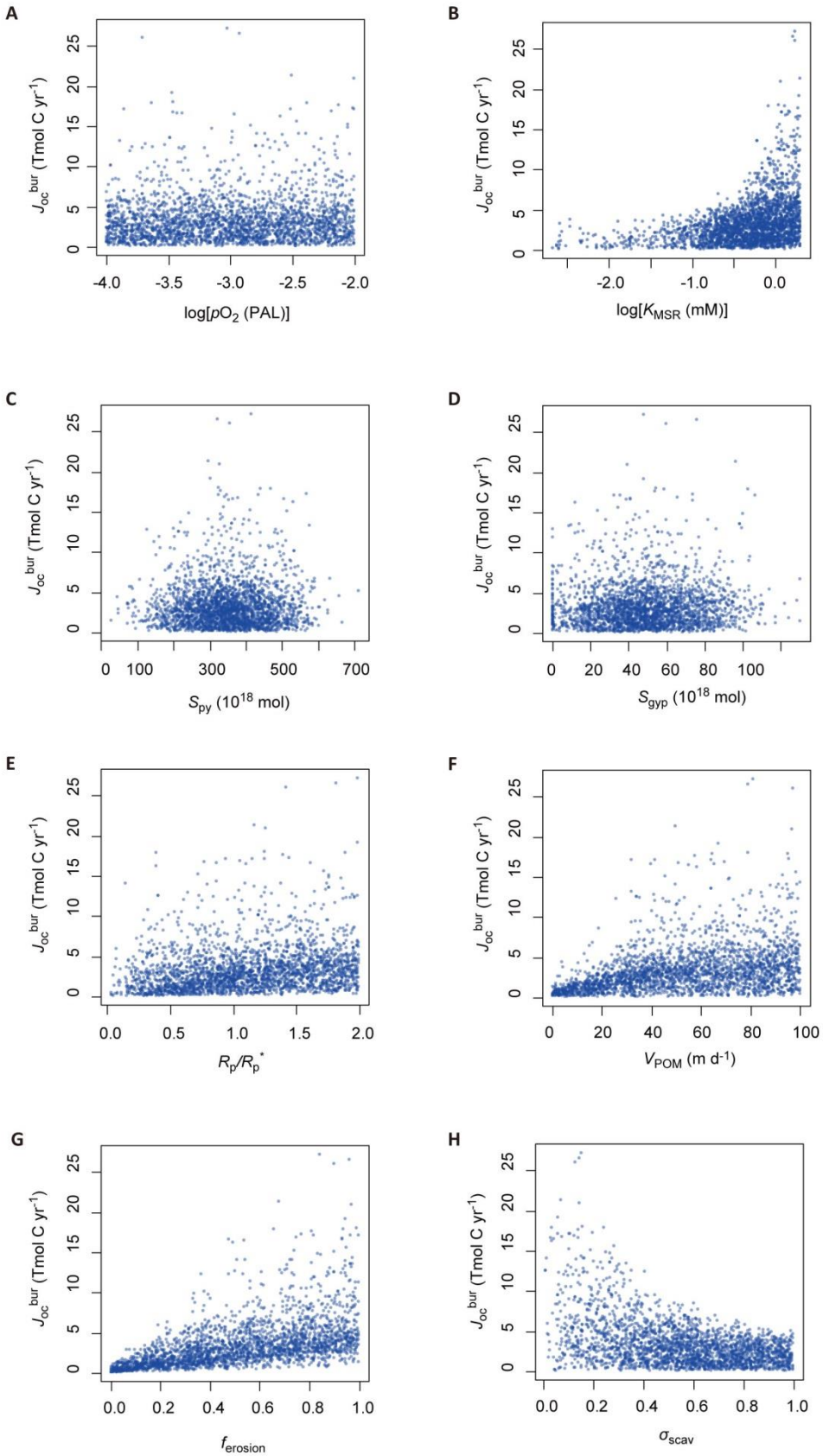

Fig. S2. Burial rate of organic carbon (J_{oc}^{bur}) vs. model parameters for the 'All' scenario. Each blue dot denotes J_{oc}^{bur} from one of 3,342 randomly-selected model runs.

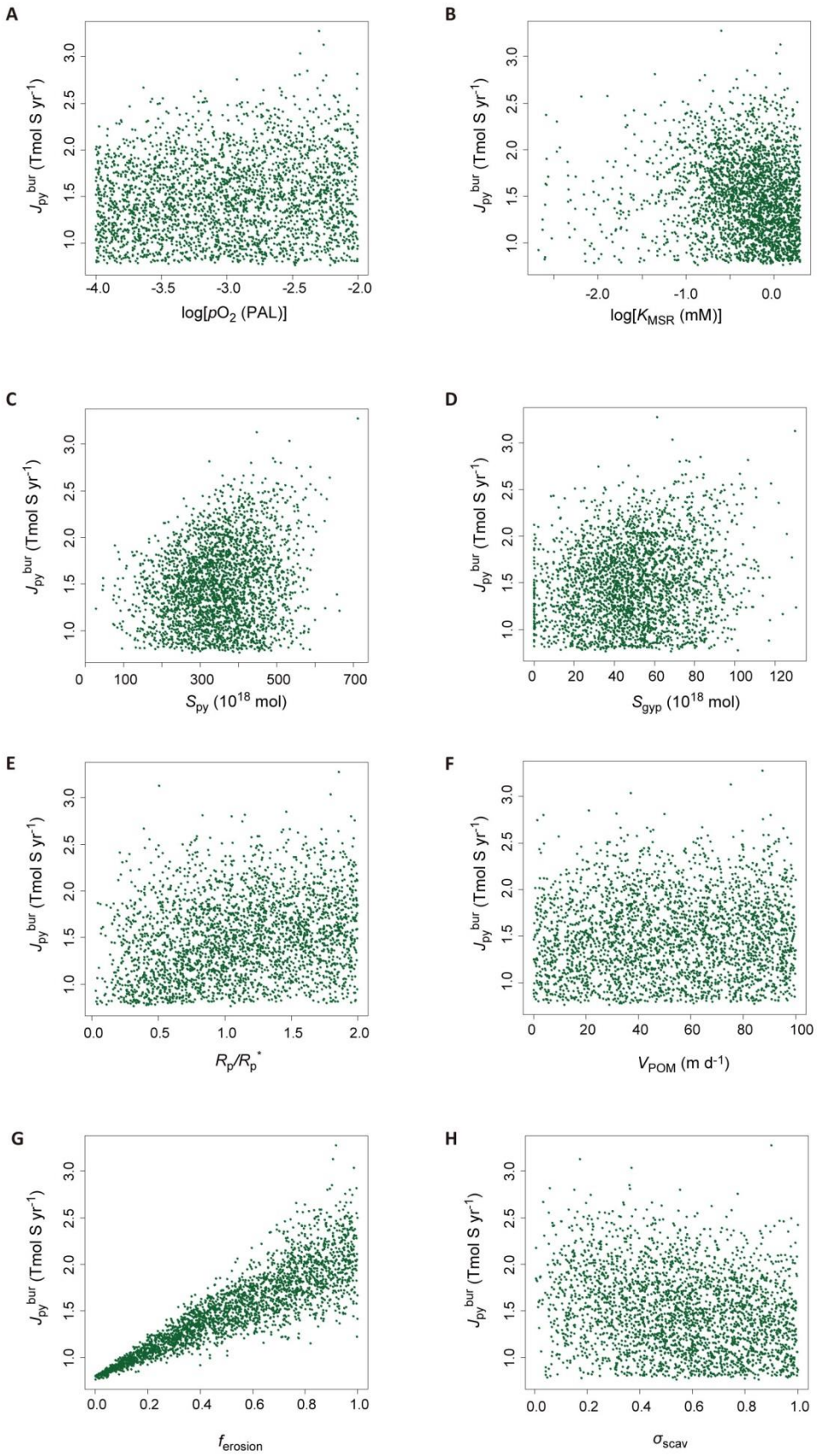

Fig. S3. Burial rate of pyrite sulphur (J_{py}^{bur}) vs. model parameters for the 'All' scenario. Each green dot denotes J_{py}^{bur} from one of 3,342 randomly-selected model runs.

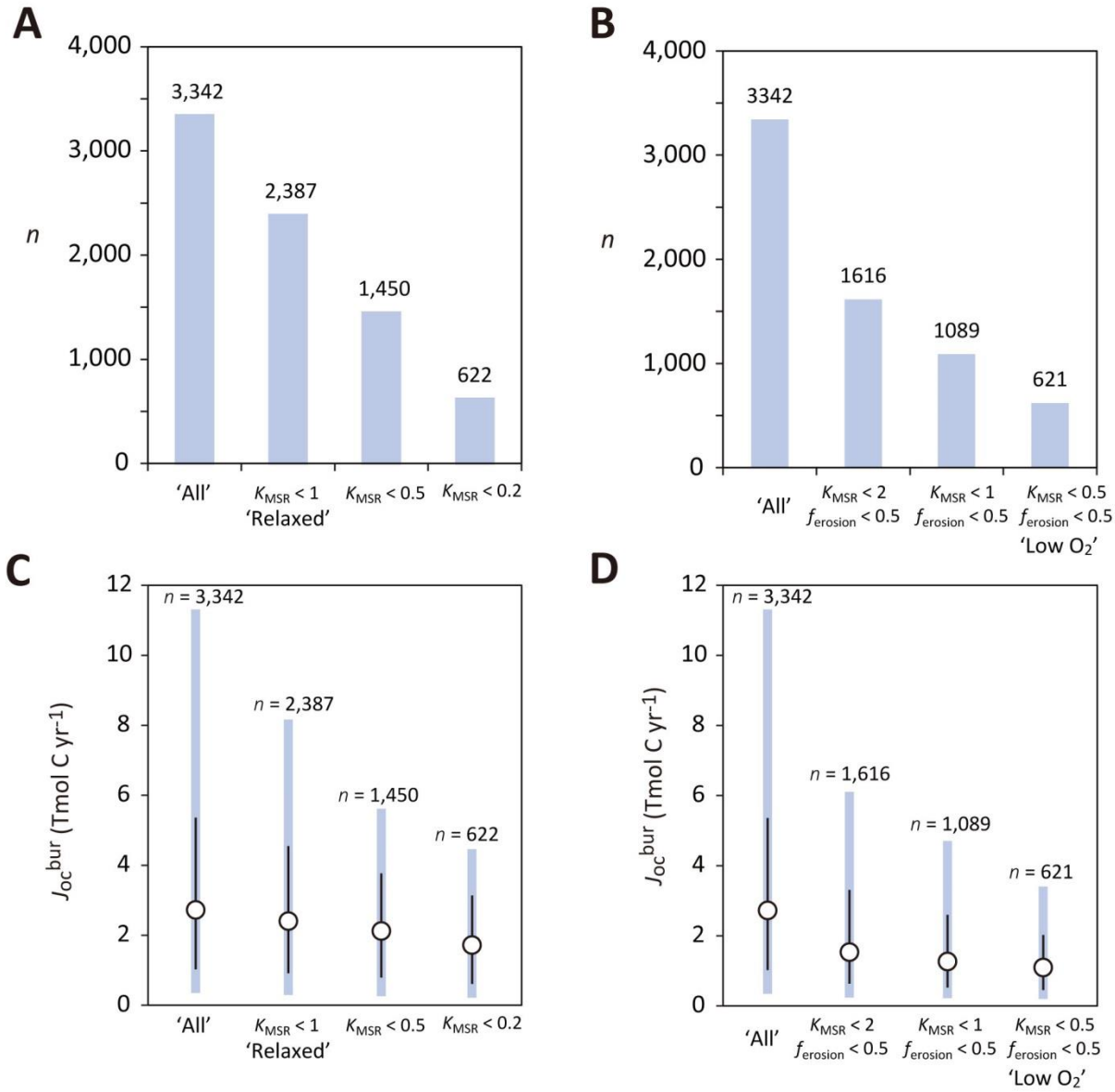

Fig. S4. The Monte Carlo simulation results showing the dependency on the upper limit of K_{MSR} and $f_{erosion}$. (a, b) The amount of data. (c, d) The burial rate of organic carbon (J_{oc}^{bur}). Error bar and shaded region denote 1σ and 95% credible intervals, respectively.

Table S1 Biogeochemical reactions considered in the CANOPS model

Process	Stoichiometry*	Reaction #
Ammonia assimilation	$\alpha CO_2 + \beta NH_4^+ + H_3PO_4 + \alpha H_2O \rightarrow OM + \alpha O_2$	R1
Nitrate assimilation	$\alpha CO_2 + \beta NO_3^- + H_3PO_4 + (\alpha+\beta)H_2O + 2\beta H^+ \rightarrow OM + (\alpha + 2\beta)O_2$	R2
Nitrogen fixation	$N_2 + 5H_2O \rightarrow 2NH_4^+ + 2OH^- + \frac{3}{2}O_2$	R3
Aerobic respiration	$OM + \alpha O_2 \rightarrow \alpha CO_2 + \beta NH_4^+ + H_3PO_4 + \alpha H_2O$	R4
Denitrification	$OM + \frac{4}{5}\alpha NO_3^- + \frac{4}{5}\alpha H^+ \rightarrow \alpha CO_2 + \beta NH_4^+ + H_3PO_4 + \frac{7}{5}\alpha H_2O + \frac{2}{5}\alpha N_2$	R5
Sulphate reduction	$OM + \frac{1}{2}\alpha SO_4^{2-} + \alpha H^+ \rightarrow \alpha CO_2 + \beta NH_4^+ + H_3PO_4 + \alpha H_2O + \frac{1}{2}\alpha H_2S$	R6
Methanogenesis	$OM \rightarrow \frac{1}{2}\alpha CO_2 + \frac{1}{2}\alpha CH_4 + \beta NH_4^+ + H_3PO_4$	R7
Nitrification	$NH_4^+ + 2O_2 \rightarrow NO_3^- + H_2O + 2H^+$	R8
Aerobic H_2S oxidation†	$\Sigma H_2S + 2O_2 \rightarrow SO_4^{2-} + 2H^+$	R9
Aerobic CH_4 oxidation	$CH_4 + 2O_2 \rightarrow CO_2 + 2H_2O$	R10
Anaerobic CH_4 oxidation	$CH_4 + SO_4^{2-} \rightarrow HS^- + HCO_3^- + H_2O$	R11
Photooxidation of CH_4	$CH_4 + 2O_2 \rightarrow CO_2 + 2H_2O$	R12
Hydrogen escape to space	$CH_4 + O_2 \rightarrow CO_2 + 4H\uparrow$	R13

*OM denotes organic matter, $(CH_2O)_\alpha(NH_4^+)_\beta H_3PO_4$

†$\Sigma H_2S = H_2S + HS^-$

Table S2 Biogeochemical formulations used in the CANOPS model

Process (unit)	Formulation*
Export/New production [mol C m^{-2} yr^{-1}]	$j_{ex}^{l,h} = \alpha^{l,h} \cdot h_m \cdot \varepsilon_{l,h} \cdot [PO_4^{3-}]_{l,h} \cdot \frac{[PO_4^{3-}]_{l,h}}{[PO_4^{3-}]_{l,h} + K_P}$
Net primary production [mol C m^{-2} yr^{-1}]	$j_{oc}^{NPP,l,h} = \frac{j_{ex}^{l,h}}{f_{ex}}$
Aerobic respiration in the water column (mol C m^{-3} yr^{-1})	$R_{O_2} = (\sum k_i G_i) \cdot \frac{[O_2]}{K_{O_2} + [O_2]}$
Denitrification in the water column [mol C m^{-3} yr^{-1}]	$R_{deni} = (\sum k_i G_i) \cdot \frac{K'_{O_2}}{K'_{O_2} + [O_2]} \cdot \frac{[NO_3^-]}{K_{NO_3} + [NO_3^-]}$
Sulphate reduction in the water column [mol C m^{-3} yr^{-1}]	$R_{MSR} = (\sum k_i G_i) \cdot \frac{K'_{O_2}}{K'_{O_2} + [O_2]} \cdot \frac{K'_{NO_3}}{K'_{NO_3} + [NO_3^-]} \cdot \frac{[SO_4^{2-}]}{K_{MSR} + [SO_4^{2-}]}$
Methanogenesis in the water column [mol C m^{-3} yr^{-1}]	$R_{methan} = (\sum k_i G_i) \cdot \frac{K'_{O_2}}{K'_{O_2} + [O_2]} \cdot \frac{K'_{NO_3}}{K'_{NO_3} + [NO_3^-]} \cdot \frac{K'_{MSR}}{K'_{MSR} + [SO_4^{2-}]}$
Aerobic respiration in sediments [mol m^{-2} yr^{-1}]	$R_{O_2}^{sed} = (1 - f_{denitr}) \times (1 - BE_{oc}) j_{oc}^{dep} \times \{1 - \exp(-kt_{OET})\}$
Benthic denitrification [μmol cm^{-2} d^{-1}]	$\log j_{denitr}^{sed} = c_0 + c_1 \log j_{oc}^{dep} + c_2 (\log j_{oc}^{dep})^2 + c_3 \log[NO_3^-]_{bw} \log[O_2]_{bw} + c_4 \log[NO_3^-]_{bw} + c_5 \log[O_2]_{bw} + c_6 \log z + c_7 \log j_{oc}^{dep} \log[O_2]_{bw}$
Sulphate reduction in sediments [mol m^{-2} yr^{-1}]	$R_{MSR}^{sed} = (1 - f_{aerobic} - f_{denitr}) \times (1 - BE_{oc}) j_{oc}^{dep} \times \frac{[SO_4^{2-}]_{bw}}{[SO_4^{2-}]_{bw} + K_{MSR}}$
Methanogenesis in sediments [mol m^{-2} yr^{-1}]	$R_{methan}^{sed} = (1 - f_{aerobic} - f_{denitr} - f_{MSR}) \times (1 - BE_{oc}) j_{oc}^{dep}$
Nitrification [mol N m^{-3} yr^{-1}]	$R_{nitrf} = k_{NH_4} \cdot [NH_4^+] \cdot [O_2]$
Aerobic H_2S oxidation† [mol S m^{-3} yr^{-1}]	$R_{H2Sox} = k_{H_2S} \cdot [\Sigma H_2S] \cdot [O_2]$
Aerobic CH_4 oxidation [mol CH_4 m^{-3} yr^{-1}]	$R_{CH_4ox} = k_{CH_4ox} \cdot [CH_4] \cdot [O_2]$
Anaerobic CH_4 oxidation [mol CH_4 m^{-3} yr^{-1}]	$R_{AOM} = k_{AOM} \cdot [CH_4] \cdot \frac{[SO_4^{2-}]}{K_{SO_4^{2-}}^{AOM} + [SO_4^{2-}]}$
Photooxidation of CH_4 [mol yr^{-1}]	$R_{CH_4ox}^{h\nu} = M_{CH_4}^{atm^{0.7}} \times \Psi_{(O_2)}$ $\Psi_{(O_2)} = 10^{a_1\psi^4 + a_2\psi^3 + a_3\psi^2 + a_4\psi + a_5}$ $\psi = \log M_{O_2}^{atm}$
Hydrogen escape to space [mol yr^{-1}]	$J_{H_{esc}} = s \times M_{CH_4}^{atm}$
C/P ratio of POM [mol mol^{-1}]	$\alpha^l = \alpha^* + \frac{\alpha^{max} - \alpha^*}{2} \left\{1 + \tanh\left(\frac{\gamma_{P0} - [PO_4^{3-}]_l}{\gamma_{P1}}\right)\right\}$
N/P ratio of POM [mol mol^{-1}]	$\beta^l = \beta^* + \frac{\beta^{max} - \beta^*}{2} \left\{1 + \tanh\left(\frac{0.1 \times 10^{-3} - [PO_4^{3-}]_l}{0.03 \times 10^{-3}}\right)\right\}$
Phosphorus scavenging [mol P m^{-2} yr^{-1}]	$j_{scav} = \sigma_{scav} \cdot J_P^{up}$

Phosphate upward flux at $z = h_m$ [mol P m^{-2} yr^{-1}]	$j_P^{up} = w \cdot [PO_4^{3-}]_{j=1} + K_z \left.\frac{\partial [PO_4^{3-}]}{\partial z}\right\|_{z=h_m}$
Oxidative weathering of organic C [mol C yr^{-1}]	$J_{oc}^{w} = f_{erosion} \cdot (pO_2(PAL))^{0.5} \cdot J_{oc}^{w,*}$
Gypsum weathering [mol S yr^{-1}]	$J_{gyp}^{w} = f_{erosion} \cdot \left(\frac{S_{gyp}}{S_{gyp}^{*}}\right) \cdot J_{gyp}^{w*}$
Total pyrite weathering [mol S yr^{-1}]	$J_{py}^{w} = J_{py}^{w\text{-abio}} + J_{py}^{w\text{-bio}}$
Abiotic pyrite weathering [mol S yr^{-1}]	$J_{py}^{w\text{-abio}} = f_{erosion} \cdot f_{O_2} \cdot \left(\frac{S_{py}}{S_{py}^{*}}\right) \cdot J_{py}^{w\text{-abio}*}$
Biotic pyrite weathering [mol S yr^{-1}]	$J_{py}^{w\text{-bio}} = f_{erosion} \cdot f_{\varepsilon} \cdot \left(\frac{S_{py}}{S_{py}^{*}}\right) \cdot J_{py}^{w\text{-bio}*}$
Riverine sulphate input rate [mol S yr^{-1}]	$J_S^{riv} = J_{gyp}^{w} + J_{py}^{w}$
Total S input rate to the system [mol S yr^{-1}]	$J_S^{in} = J_S^{riv} + J_S^{vol} + J_S^{MOR}$
Gypsum deposition [mol S yr^{-1}]	$J_{gyp}^{bur} = J_{gyp}^{bur*} \times \frac{[Ca^{2+}]_l [SO_4^{2-}]_l}{[Ca^{2+}]^{*} [SO_4^{2-}]^{*}}$
Sedimentary pyrite precipitation rate [mol S m^{-2} yr^{-1}]	$j_{py}^{bur} = e_{py} \times j_{H_2S}$
Pyrite burial efficiency	$e_{py} = e_{py}^{max} - (e_{py}^{max} - e_{py}^{*}) \times \tanh\left(\frac{[O_2]_{bw}}{1\,\mu M}\right)$
H_2S production rate at the sediment-water interface [mol S m^{-2} yr^{-1}]	$j_{H_2S} = \frac{1}{2} f_{MSR} (1 - BE_{oc}) j_{oc}^{dep} + j_{AOM}$
Depositional flux density of particulate organic carbon [mol C m^{-2} yr^{-1}]	$j_{oc}^{dep} = v_{POM} \times (\Sigma G_i)$
Burial efficiency of organic carbon [%]	$BE_{oc} = \frac{be_1 - be_2}{1 + SR/a} + be_2$
Burial efficiency of organic phosphorus	$BE_{Porg} = BE_{oc} \frac{\alpha}{(C_{org}/P_{org})_{bur}}$
Burial efficiency of authigenic P	$BE_{Pauth} = 2 \times BE_{Porg}$
Burial efficiency of Fe-bound P	$BE_{PFe} = \begin{cases} BE_{Porg} \frac{[O_2]_{bw}}{oxic} & \text{for } [O_2]_{bw} < oxic \\ BE_{Porg} & \text{for } [O_2]_{bw} \geq oxic \end{cases}$
C_{org}/P_{org} of buried sediments for $[O_2]_{bw}$ < oxic [mol/mol]	$(C_{org}/P_{org})_{bur} = \frac{2\alpha (C_{org}/P_{org})_{bur}^{anox}}{(C_{org}/P_{org})_{bur}^{anox} \frac{[O_2]_{bw}}{oxic} + \left(1 - \frac{[O_2]_{bw}}{oxic}\right) 2\alpha} \frac{1 + \exp(-\tau_{bur}/10000)}{2}$
C_{org}/P_{org} of buried sediments for $[O_2]_{bw}$ ≧ oxic [mol/mol]	$(C_{org}/P_{org})_{bur} = 2\alpha \frac{1 + \exp(-\tau_{bur}/10000)}{2}$
Time scale constant for burial [yr]	$\tau_{bur} = \frac{10}{w}$

Burial flux density of organic C [mol C m^{-2} yr^{-1}]	$j_{\mathrm{oc}}^{\mathrm{bur}} = BE_{\mathrm{oc}} \times j_{\mathrm{oc}}^{\mathrm{dep}}$
Burial flux density of organic P [mol P m^{-2} yr^{-1}]	$j_{\mathrm{Porg}}^{\mathrm{bur}} = BE_{\mathrm{Porg}} / \alpha \times j_{\mathrm{oc}}^{\mathrm{dep}}$
Oxygen penetration depth [cm]	$\log \mathrm{OPD} = a_0 + a_1 \log w + a_2 \log[\mathrm{O}_2]_{\mathrm{bw}} + a_3 \log j_{\mathrm{oc}}^{\mathrm{dep}} + a_4 (\log w)^2 + a_5 (\log[\mathrm{O}_2]_{\mathrm{bw}})^2 + a_6 (\log j_{\mathrm{oc}}^{\mathrm{dep}})^2 + a_7 (\log w)(\log[\mathrm{O}_2]_{\mathrm{bw}}) + a_8 (\log[\mathrm{O}_2]_{\mathrm{bw}})(\log j_{\mathrm{oc}}^{\mathrm{dep}}) + a_9 (\log w)(\log j_{\mathrm{oc}}^{\mathrm{dep}}) + a_{10} T_{\mathrm{bw}}$
Oxygen exposure time [yr]	$t_{\mathrm{OET}} = \dfrac{\mathrm{OPD}}{w}$

[*] *l* and *h* represent low- and high-latitude surface layer, respectively. *z* is water depth, and *w* is upwelling rate at $z = h_{\mathrm{m}}$.

Table S3 Parameter values in the CANOPS model. Numbers in parentheses denote the reference value.

Parameter [unit]	Value
Physical parameters	
Ocean surface area, A_{oc} [m^2]	3.62×10^{14}
Surface area of high-latitude layer (H), A_{oc}^{H} [m^2]	0.362×10^{14}
Depth of mixed layer, h_m [m]	100
Grid spacing, Δz [m]	100
Water depth of ocean bottom, z_b [m]	6,100
Ocean overturning rate, V [Sv]	20
Vertical mixing coefficient (z < 500 m), K_u [m^2 yr^{-1}]	5,000
Vertical mixing coefficient (500 m < z < 1,500 m), K_l [m^2 yr^{-1}]	2,500
Mixing coefficient, κ_s [m^2 yr^{-1}]	473
Mixing coefficient, κ_d [m^2 yr^{-1}]	3,154
Transition depth for vertical mixing coefficient, z_l	1,000
High-latitude convection rate, V_h [Sv]	57.4
Horizontal diffusion coefficient, K_{hor} [m^2 s^{-1}]	1,000
Sea surface temperature at low-mid latitude region, SST^l [°C]	15
Sea surface temperature at high latitude region, SST^h [°C]	0
Sea surface salinity at low-mid latitude region, SSS^l [psu]	35.5
Sea surface salinity at high latitude region, SST^h [psu]	34.5
Biogeochemical parameters	
Efficiency factor for phosphate uptake at L, ε^l	1.0
Efficiency factor for phosphate uptake at H, ε^h	0.15
Phosphate half saturation constant, K_P [mM]	1×10^{-6}
Reference value of export ratio, $f$ex*	0.2
Redfield ratio for C/P, α^* [mol mol^{-1}]	106
Redfield ratio for N/P, β^* [mol mol^{-1}]	16
Stoichiometric C/P ratio upper limit, α_{max} [mol mol^{-1}]	400
Stoichiometric C/N ratio upper limit, β_{max} [mol mol^{-1}]	60
C/N/P stoichiometry constant, γ_{P0} [mM]	0.1
C/N/P stoichiometry constant, γ_{P1}[mM]	0.03
C_{org}/N_{org} ratio of buried sediments, $(C/N)_{bur}$ [mol mol^{-1}]	10
Reference value of riverine reactive P input rate, R_P^* [Tmol P yr^{-1}]	0.18
Riverine nitrate input rate, R_N [Tg N yr^{-1}]	0 (40.3)
Atmospheric deposition of reactive nitrogen, A_N [Tg N yr^{-1}]	0
Sulphur input rate via aerobic volcanisms, J_S^{vol} [Tmol S yr^{-1}]	0.7
H_2S input rate via submarine volcanisms, J_S^{MOR} [Tmol S yr^{-1}]	0.1
Present riverine sulphate input flux, J_S^{riv*} [Tmol S yr^{-1}]	2.6
Present gypsum weathering flux, J_{gyp}^{w*} [Tmol S yr^{-1}]	1.95
Present pyrite weathering flux, J_{py}^{w*} [Tmol S yr^{-1}]	0.65
Present biotic pyrite weathering flux, $J_{py}^{w\text{-}bio*}$ [Tmol S yr^{-1}]	0.26
Present abiotic pyrite weathering flux, $J_{py}^{w\text{-}abio*}$ [Tmol S yr^{-1}]	0.39
Present crustal reservoir size of gypsum S, S_{gyp}^* [10^{18} mol S]	200
Present crustal reservoir size of pyrite S, S_{py}^* [10^{18} mol S]	200
Biotic enhancement factor for pyrite weathering, f_ε	0.8 (1.0)
Reference value for gypsum deposition rate, J_{gyp}^{bur*} [Tmol S yr^{-1}]	2.1
Seawater calcium ion concentration, [Ca^{2+}] [mM]	10.54
Reference value of sulphate concentration, [SO_4^{2-}]* [mM]	28.9

Reference value of pyrite burial efficiency, e_{py}^{*}	0.13
Maximum value of pyrite burial efficiency, e_{py}^{max}	1.0
Reference value of POM sinking velocity, v_{POM}^{*} [m d^{-1}]	100
Decomposition rate of G_1, k_1 [d^{-1}]	0.6
Decomposition rate of G_2, k_2 [d^{-1}]	0.1
Decomposition rate of G_3, k_3 [d^{-1}]	0.0
Mass fraction of G_1, m_1	0.72
Mass fraction of G_2, m_1	0.25
Mass fraction of G_3, m_1	0.03
Scale constant for benthic aerobic respiration, k [yr^{-1}]	0.02
Burial efficiency of organic C at zero sediment accumulation rate, be_1 [%]	0.5 for $[O_2]_{bw}$ >200 μM 5.0 for $[O_2]_{bw}$ <30 μM
Burial efficiency of organic C at infinite sediment accumulation rate, be_2 [%]	75
Centre of the regression for burial efficiency of organic C, a [g cm^{-2} yr^{-1}]	0.07 for $[O_2]_{bw}$ >200 μM 0.01 for $[O_2]_{bw}$ <30 μM
Reference value of $[O_2]_{bw}$ for burial efficiency of organic P, oxic [mM]	0.25
Half saturation constant for aerobic respiration, K_{O2} [mM]	8×10^{-3}
Half saturation constant for denitrification, K_{NO3} [mM]	3×10^{-2}
Reference value of half saturation constant for MSR, K_{MSR}^{*} [mM]	0.065
Half saturation constant for AOM, K_{SO4}^{AOM} [mM]	0.093
Aerobic oxidation rate of ammonium, k_{NH4OX} [mM^{-1} yr^{-1}]	1.825×10^{4}
Aerobic oxidation rate of sulphide, k_{H2SOX} [mM^{-1} yr^{-1}]	3.65×10^{3}
Aerobic methane oxidation rate, k_{CH4OX} [mM^{-1} yr^{-1}]	1×10^{7}
Anaerobic methane oxidation rate, k_{AOM} [yr^{-1}]	3×10^{-4}
Piston velocity of O_2, v_{O2}^{piston} [m yr^{-1}]	300
Piston velocity of H_2S, v_{H2S}^{piston} [m yr^{-1}]	1,072
Piston velocity of CH_4, v_{CH4}^{piston} [m yr^{-1}]	1,419
Piston velocity of NH_3, v_{NH3}^{piston} [m yr^{-1}]	300
Solubility of H_2S at 25°C, $K_{H2S}^{Henry^{\circ}}$ [mol m^{-3} bar^{-1}]	100
Solubility of CH_4 at 25°C, $K_{CH4}^{Henry^{\circ}}$ [mol m^{-3} bar^{-1}]	1.4
Solubility of NH_3 at 25°C, $K_{NH3}^{Henry^{\circ}}$ [mol m^{-3} bar^{-1}]	5.6×10^{4}
Temperature dependence of solubility of H_2S, K_{H2S}^{T} [K]	2,100
Temperature dependence of solubility of CH_4, K_{CH4}^{T} [K]	1,600
Temperature dependence of solubility of NH_3, K_{NH3}^{T} [K]	4,100
Sea surface pH at low-mid latitude region, pH^{l}	8.17
Sea surface pH at high latitude region, pH^{h}	8.16
Partial pressure of atmospheric pH_2S, pH_2S [atm]	0.0
Partial pressure of atmospheric pNH_3, pNH_3 [atm]	0.0
Coefficients for photooxidation of CH_4, a_1	0.0030084
Coefficients for photooxidation of CH_4, a_2	-0.1655405
Coefficients for photooxidation of CH_4, a_3	3.2305351
Coefficients for photooxidation of CH_4, a_4	-25.8343054
Coefficients for photooxidation of CH_4, a_5	71.5397861
Scale constant for hydrogen escape, s [yr^{-1}]	3.7×10^{-5}

Table S4 Globally integrated flux for the reference run of the CANOPS model

Parameter	Units	This study
Fluxes		
Export production, *EX*	Gt C yr^{-1}	8.92
Net primary production, *NPP*	Gt C yr^{-1}	44.6
Nitrogen fixation, J_{Nfix}	Tg N yr^{-1}	136
Depositional flux of organic carbon	Tmol C yr^{-1}	0.84
Denitrification in the water column	Tg N yr^{-1}	100
Denitrification in the sediments	Tg N yr^{-1}	61
MSR in marine sediments, J_{MSR}^{sed}	Tmol S yr^{-1}	10.1
Organic carbon burial, J_{oc}^{bur}	Tmol C yr^{-1}	11.95
Organic nitrogen burial, J_{N}^{bur}	Tg N yr^{-1}	16.7
Burial rate of organic P, J_{Porg}^{bur}	Tmol P yr^{-1}	0.047
Burial rate of authigenic P, J_{Pauth}^{bur}	Tmol P yr^{-1}	0.094
Burial rate of Fe-bound P, J_{PFe}^{bur}	Tmol P yr^{-1}	0.039
C_{org}/P_{react} of buried sediments	mol mol^{-1}	66.4
Burial rate of pyrite sulphur, J_{py}^{bur}	Tmol S yr^{-1}	1.3
Gypsum deposition rate, J_{gyp}^{bur}	Tmol S yr^{-1}	2.1
Inventory		
Marine phosphate inventory, M_P	10^{15} mol	2.67
Marine nitrate inventory, M_N	10^{15} mol	32.2
Marine dissolved O_2 inventory, M_{O2}	10^{18} mol	0.23
Marine sulphate inventory, M_{SO4}	10^{18} mol	38
$[SO_4^{2-}]$ at L	mM	28.3
Residence time of DIP	kyr	15

Table S5 Parameter ranges used in our Monte Carlo analysis

Sampled parameters	Scenario				Sampling method
	All (n = 3,342)	Relaxed (n = 2,385)	Low O_2 (n = 621)	High O_2 (n = 308)	
Atmospheric oxygen level, pO_2 (PAL)	0.01–1%	0.01–1%	0.01–1%	1–10%	Log uniform
Half-saturation constant for MSR, K_{MSR} (mM)	0.002–2	0.002–1	0.002–0.5	0.002–0.5	Log uniform
Riverine reactive P input rate, R_P (normalized)[†]	0–200%	0–200%	0–200%	0–200%	Uniform
Phosphorus scavenging efficiency, σ_{scav}	0–1	0–1	0–1	0–1	Uniform
Total crustal sulphur reservoir size, S_{py}+S_{gyp} (10^{18} mole)	400±100 (1σ)	400±100 (1σ)	400±100 (1σ)	400±100 (1σ)	Gaussian
Crustal gypsum sulphur reservoir size, S_{gyp} (10^{18} mole)	50±25 (1σ)	50±25 (1σ)	50±25 (1σ)	50±25 (1σ)	Gaussian
Sinking velocity of POM, V_{POM} (m d^{-1})	0–100	0–100	0–100	0–100	Uniform
Global erosion/sedimentation rate, $f_{erosion}$ (normalized)[‡]	0–1.0	0–1.0	0–0.5	0–0.5	Uniform

[†]The modern value is 0.18 Tmol P yr^{-1}.

[‡]$f_{erosion}$ = 1 for the present.

Table S6. Monte Carlo simulation results for ‘Low O_2’, ‘Relaxed’ and ‘High O_2’ scenarios

	Low O_2 (n = 621)			
	Mean	Median	68% credible interval	95% credible interval
Organic carbon burial rate, J_{oc}^{bur} [Tmol C yr^{-1}]	1.25	1.10	0.45–2.03	0.20–3.41
Pyrite sulphur burial rate, J_{py}^{bur} [Tmol S yr^{-1}]	1.19	1.18	0.93–1.44	0.81–1.63
Net O_2 production rate, J_{O2} [Tmol O_2 yr^{-1}]	3.66	3.51	2.39–4.88	1.85–6.44
Marine P inventory, M_P [%POL]	3.53	3.19	1.93–5.07	1.35–7.30
Organic C export production, EX [Gt C yr^{-1}]	1.17	1.06	0.61–1.68	0.42–2.47
Nitrogen fixation, J_{Nfix} [Tg N yr^{-1}]	23.0	21.3	10.0–34.5	6.52–51.7
CH_4 degassing flux to the atmosphere, log(J_{CH4} [Tmol yr^{-1}])	1.95	2.10	1.58–2.40	0.42–2.56
Atmospheric CH_4 mixing ratio, log($f$$CH_4$ [ppmv])	0.36	0.53	-0.25–1.07	-1.90–1.45
Relative significance of J_{py}^{bur} and J_{oc}^{bur} in the O_2 production, O_{2py}/O_{2oc}	2.84	2.17	1.34–4.40	0.85–8.04
Φ_{out}(Red) [Tmol O_2 equiv. yr^{-1}]	2.09	1.94	1.26–2.89	1.00–4.35
	Relaxed (n = 2,385)			
	Mean	Median	68% credible interval	95% credible interval
Organic carbon burial rate, J_{oc}^{bur} [Tmol C yr^{-1}]	2.79	2.40	0.92–4.54	0.30–8.16
Pyrite sulphur burial rate, J_{py}^{bur} [Tmol S yr^{-1}]	1.53	1.50	1.05–1.99	0.83–2.41
Net O_2 production rate, J_{O2} [Tmol O_2 yr^{-1}]	5.91	5.55	3.20–8.43	2.02–12.4
Marine P inventory, M_P [%POL]	5.32	4.96	2.91–7.47	1.68–11.2
Organic C export production, EX [Gt C yr^{-1}]	1.76	1.61	0.94–2.48	0.53–4.03
Nitrogen fixation, J_{Nfix} [Tg N yr^{-1}]	33.1	28.9	15.9–48.9	8.23–81.6
CH_4 degassing flux to the atmosphere, log(J_{CH4} [Tmol yr^{-1}])	2.22	2.32	1.96–2.55	0.79–2.73
Atmospheric CH_4 mixing ratio, log($f$$CH_4$ [ppmv])	0.74	0.84	0.27–1.32	-1.19–1.71
Relative significance of J_{py}^{bur} and J_{oc}^{bur} in the O_2 production, O_{2py}/O_{2oc}	1.75	1.31	0.77–2.59	0.47–6.01
Φ_{out}(Red) [Tmol O_2 equiv. yr^{-1}]	3.56	3.14	1.68–5.40	1.07–9.03
	High O_2 (n = 308)			
	Mean	Median	68% credible interval	95% credible interval
Organic carbon burial rate, J_{oc}^{bur} [Tmol C yr^{-1}]	1.94	1.64	0.66–3.16	0.31–5.26
Pyrite sulphur burial rate, J_{py}^{bur} [Tmol S yr^{-1}]	1.15	1.14	0.89–1.39	0.80–1.58
Net O_2 production rate, J_{O2} [Tmol O_2 yr^{-1}]	4.33	4.07	2.66–5.97	2.04–8.18
Marine P inventory, M_P [%POL]	5.15	4.76	3.32–7.00	2.53–9.20
Organic C export production, EX [Gt C yr^{-1}]	1.70	1.58	1.09–2.33	0.81–3.16
Nitrogen fixation, J_{Nfix} [Tg N yr^{-1}]	74.3	62.5	37.5–114	23.7–183
CH_4 degassing flux to the atmosphere, log(J_{CH4} [Tmol yr^{-1}])	1.86	2.00	1.41–2.27	0.33–2.45
Atmospheric CH_4 mixing ratio, log($f$$CH_4$ [ppmv])	0.93	1.12	0.32–1.53	-1.29–1.79
Relative significance of J_{py}^{bur} and J_{oc}^{bur} in the O_2 production, O_{2py}/O_{2oc}	1.90	1.39	0.78–3.18	0.49–6.28
Φ_{out}(Red) [Tmol O_2 equiv. yr^{-1}]	0.19	0.38	-1.11–1.34	-2.60–2.24

Table S7 The oxidizing power of various species in units scaled to the oxidizing power of O_2 that is defined as +1

Species	Oxidizing power
H_2O	0
CO_2	0
N_2	0
FeO	0
H_2SO_4	0
O_2	+1
H_2	-0.5
CH_4	-2
CH_2O	-1
CO	-0.5
NH_3	-0.75
HNO_3	+1.25
$Fe(OH)_3$	+0.25
H_2S	-2
SO_2	-0.5

Table S8 Carbon isotope model.

Description	Standard	Low O_2	High O_2
Isotopic value of DIC, δ [‰]	0	0	0
Isotopic value of mantle, δ_{mantle} [‰]	-5	-5	-5
Isotopic value of crustal organic carbon, δ_{oc}^{w} [‰]	-25	-25	-25
Isotopic value of crustal carbonate, δ_{carb}^{w} [‰]	0	0	0
Isotopic fractionation between organic matter and DIC, Δ [‰]	25	25	25
Carbon outgassing rate from the mantle, J_{mantle} [Tmol C yr^{-1}]	2	3	3
Oxidative weathering rate of organic carbon, J_{oc}^{w} [Tmol C yr^{-1}]	10	0.164†	2.22†
Carbonate weathering rate, J_{carb}^{w} [Tmol C yr^{-1}]	40	60	60
Burial rate of organic carbon, J_{oc}^{bur} [Tmol C yr^{-1}]	10	1.25†	1.94†
Isotopic value of total carbon input flux, δ_{in} [‰]	-5	-0.30	-1.08
Fraction of carbon buried as organic carbon, f_{org}	0.2	0.012	0.043

†From our Monte Carlo simulations (Fig. 5 and Table S6).

References

Algeo TJ, Ingall E (2007) Sedimentary Corg:P ratios, paleocean ventilation, and Phanerozoic atmospheric pO2. *Palaeogeogr. Palaeoclimatol. Palaeoecol.*, **256**, 130-155.

Baturin GN (2007) Issue of the relationship between primary productivity of organic carbon in ocean and phosphate accumulation (Holocene-Late Jurassic). *Lithology and Mineral Resources*, **42**, 318-348.

Beal EJ, Claire MW, House CH (2011) High rates of anaerobic methanotrophy at low sulfate concentrations with implications for past and present methane levels. *Geobiology*, **9**, 131-139.

Bekker A, Holland HD, Wang PL, Rumble Iii D, Stein HJ, Hannah JL, Coetzee LL, Beukes NJ (2004) Dating the rise of atmospheric oxygen. *Nature*, **427**, 117.

Bergman NM, Lenton TM, Watson AJ (2004) COPSE: A new model of biogeochemical cycling over Phanerozoic time. *Am. J. Sci.*, **304**, 397-437.

Berner RA (1980) *Early diagenesis: A theoretical approach*, Princeton University Press, Princeton.

Berner RA (1982) Burial of organic carbon and pyrite sulfur in the modern ocean; its geochemical and environmental significance. *Am. J. Sci.*, **282**, 451-473.

Berner RA (2004) A model for calcium, magnesium and sulfate in seawater over Phanerozoic time. *Am. J. Sci.*, **304**, 438-453.

Berner RA (2006) GEOCARBSULF: A combined model for Phanerozoic atmospheric O_2 and CO_2. *Geochim. Cosmochim. Acta*, **70**, 5653-5664.

Berner RA (2009) Phanerozoic atmospheric oxygen: New results using the GEOCARBSULF model. *Am. J. Sci.*, **309**, 603-606.

Berner RA, Canfield DE (1989) A new model for atmospheric oxygen over Phanerozoic time. *Am. J. Sci.*, **289**, 333-361.

Berner RA, Westrich JT (1985) Bioturbation and the early diagenesis of carbon and sulfur. *Am. J. Sci.*, **285**, 193-206.

Bohlen L, Dale AW, Wallmann K (2012) Simple transfer functions for calculating benthic fixed nitrogen losses and C:N:P regeneration ratios in global biogeochemical models. *Glob. Biogeochem. Cycles*, **26**, n/a-n/a.

Bottrell SH, Newton RJ (2006) Reconstruction of changes in global sulfur cycling from marine sulfate isotopes. *Earth-Science Reviews*, **75**, 59-83.

Bowles MW, Mogollón JM, Kasten S, Zabel M, Hinrichs K-U (2014) Global rates of marine sulfate reduction and implications for sub–sea-floor metabolic activities. *Science*, **344**, 889-891.

Brandes JA, Devol AH (2002) A global marine-fixed nitrogen isotopic budget: Implications for Holocene nitrogen cycling. *Glob. Biogeochem. Cycles*, **16**, 67-61-67-14.

Burdige DJ (2005) Burial of terrestrial organic matter in marine sediments: A re-assessment. *Glob. Biogeochem. Cycles*, **19**.

Burdige DJ (2007) Preservation of Organic Matter in Marine Sediments: Controls, Mechanisms, and an Imbalance in Sediment Organic Carbon Budgets? *Chemical Reviews*, **107**, 467-485.

Canfield DE (1989) Sulfate reduction and oxic respiration in marine sediments: implications for organic carbon preservation in euxinic environments. *Deep Sea Research Part A. Oceanographic Research Papers*, **36**, 121-138.

Canfield DE (1991) Sulfate reduction in deep-sea sediments. *Am. J. Sci.*, **291**, 177-188.

Canfield DE (2004) The evolution of the Earth surface sulfur reservoir. *Am. J. Sci.*, **304**, 839-861.

Canfield DE, Farquhar J (2009) Animal evolution, bioturbation, and the sulfate concentration of the oceans. *Proc Natl Acad Sci U S A*, **106**, 8123-8127.

Canfield DE, Habicht KS, Thamdrup B (2000) The Archean Sulfur Cycle and the Early History of Atmospheric Oxygen. *Science*, **288**, 658-661.

Catling DC, Kasting JF (2017) *Atmospheric Evolution on Inhabited and Lifeless Worlds*, Cambridge University Press.

Cawood PA, Hawkesworth CJ (2014) Earth's middle age. *Geology*, **42**, 503-506.

Cole DB, Reinhard CT, Wang X, Gueguen B, Halverson GP, Gibson T, Hodgskiss MSW, Mckenzie NR, Lyons TW, Planavsky NJ (2016) A shale-hosted Cr isotope record of low atmospheric oxygen during the Proterozoic. *Geology*.

Colman AS, Holland HD (2000) The global diagenetic flux of phosphorus from marine sediments to the oceans: redox sensitivity and the control of atmosphreic oxygen levels. In: *Marine authigenesis: from global to microbial* (eds Glenn CR, Prevot-Lucas L, Lucas J). SEPM (Society for Sedimentary Geology).

Compton J, Mallinson D, Glenn CR, Filippelli G, Follmi K, Shields GA, Zanin Y (2000) Variations in the global phosphorus cycle. In: *Marine authigenesis: from global to microbial* (eds Glenn CR, Prevot-Lucas L, Lucas J). SEPM (Society for Sedimentary Geology), pp. 21-33.

Daines SJ, Mills BJW, Lenton TM (2017) Atmospheric oxygen regulation at low Proterozoic levels by incomplete oxidative weathering of sedimentary organic carbon. *Nature Commun.*, **8**, 14379.

Dale AW, Meyers SR, Aguilera DR, Arndt S, Wallmann K (2012) Controls on organic carbon and molybdenum accumulation in Cretaceous marine sediments from the Cenomanian–Turonian interval including Oceanic Anoxic Event 2. *Chem. Geol.,* **324–325**, 28-45.

Delaney ML (1998) Phosphorus accumulation in marine sediments and the oceanic phosphorus cycle. *Glob. Biogeochem. Cycles,* **12**, 563-572.

Deutsch C, Sarmiento JL, Sigman DM, Gruber N, Dunne JP (2007) Spatial coupling of nitrogen inputs and losses in the ocean. *Nature,* **445**, 163.

Devol AH (2015) Denitrification, Anammox, and N2 Production in Marine Sediments. *Ann. Rev. Mar. Sci.,* **7**, 403-423.

Devries T, Deutsch C, Primeau F, Chang B, Devol A (2012) Global rates of water-column denitrification derived from nitrogen gas measurements. *Nat. Geosci.,* **5**, 547.

Devries T, Deutsch C, Rafter PA, Primeau F (2013) Marine denitrification rates determined from a global 3-D inverse model. *Biogeosciences,* **10**, 2481-2496.

Duce RA, Laroche J, Altieri K, Arrigo KR, Baker AR, Capone DG, Cornell S, Dentener F, Galloway J, Ganeshram RS, Geider RJ, Jickells T, Kuypers MM, Langlois R, Liss PS, Liu SM, Middelburg JJ, Moore CM, Nickovic S, Oschlies A, Pedersen T, Prospero J, Schlitzer R, Seitzinger S, Sorensen LL, Uematsu M, Ulloa O, Voss M, Ward B, Zamora L (2008) Impacts of Atmospheric Anthropogenic Nitrogen on the Open Ocean. *Science,* **320**, 893-897.

Dunne JP, Sarmiento JL, Gnanadesikan A (2007) A synthesis of global particle export from the surface ocean and cycling through the ocean interior and on the seafloor. *Glob. Biogeochem. Cycles,* **21**, n/a-n/a.

Eugster O, Gruber N (2012) A probabilistic estimate of global marine N-fixation and denitrification. *Glob. Biogeochem. Cycles,* **26**.

Farquhar J, Bao H, Thiemens M (2000) Atmospheric Influence of Earth's Earliest Sulfur Cycle. *Science,* **289**, 756-758.

Fiebig J, Woodland AB, D'alessandro W, Püttmann W (2009) Excess methane in continental hydrothermal emissions is abiogenic. *Geology,* **37**, 495-498.

Fowler D, Coyle M, Skiba U, Sutton MA, Cape JN, Reis S, Sheppard LJ, Jenkins A, Grizzetti B, Galloway JN, Vitousek P, Leach A, Bouwman AF, Butterbach-Bahl K, Dentener F, Stevenson D, Amann M, Voss M (2013) The global nitrogen cycle in the twenty-first century. *Phil. Trans. R. Soc. B,* **368**.

Galloway JN, Dentener FJ, Capone DG, Boyer EW, Howarth RW, Seitzinger SP, Asner GP, Cleveland CC, Green PA, Holland EA, Karl DM, Michaels AF, Porter JH, Townsend AR, Vöosmarty CJ (2004) Nitrogen Cycles: Past, Present, and Future. *Biogeochemistry,* **70**, 153-226.

Garcia HE, Gordon LI (1992) Oxygen solubility in seawater: Better fitting equations. *Limnology and Oceanography,* **37**, 1307-1312.

Garrels RM, Mackenzie, F. T. (1971) *Evolution of Sedimentary Rocks,* W. W. NORTON & CO., New York.

Goldblatt C, Lenton TM, Watson AJ (2006) Bistability of atmospheric oxygen and the Great Oxidation. *Nature,* **443**, 683-686.

Großkopf T, Mohr W, Baustian T, Schunck H, Gill D, Kuypers MMM, Lavik G, Schmitz RA, Wallace DWR, Laroche J (2012) Doubling of marine dinitrogen-fixation rates based on direct measurements. *Nature,* **488**, 361.

Gruber N (2008) Chapter 1 - The Marine Nitrogen Cycle: Overview and Challenges. In: *Nitrogen in the Marine Environment (2nd Edition).* Academic Press, San Diego, pp. 1-50.

Gruber N, Sarmiento JL (1997) Global patterns of marine nitrogen fixation and denitrification. *Glob. Biogeochem. Cycles,* **11**, 235-266.

Gruber N, Sarmiento JL (2002) Biogeochemical/physical interactions in elemental cycles. In: *THE SEA: Biological-Physical Interactions in the Oceans* (eds Robinson AR, Mccarthy JJ, Rothschild BJ). John Wiley and Sons, New York, pp. 337-399.

Guidry MW, Mackenzie FT, Arvidson RS (2000) Role of tectonics in phosphorus distribution and cycling. In: *Marine Authigenesis: From Global to Microbial* (eds Glenn CR, Prevot-Lucas L, Lucas J). SEPM, pp. 35-51.

Hardie LA (2003) Secular variations in Precambrian seawater chemistry and the timing of Precambrian aragonite seas and calcite seas. *Geology,* **31**, 785-788.

Hardisty DS, Lu Z, Bekker A, Diamond CW, Gill BC, Jiang G, Kah LC, Knoll AH, Loyd SJ, Osburn MR, Planavsky NJ, Wang C, Zhou X, Lyons TW (2017) Perspectives on Proterozoic surface ocean redox from iodine contents in ancient and recent carbonate. *Earth Planet. Sci. Lett.,* **463**, 159-170.

Heinze C, Kriest I, Maier-Reimer E (2009) Age offsets among different biogenic and lithogenic components of sediment cores revealed by numerical modeling. *Paleoceanography,* **24**, n/a-n/a.

Herman F, Seward D, Valla PG, Carter A, Kohn B, Willett SD, Ehlers TA (2013) Worldwide acceleration of mountain erosion under a cooling climate. *Nature,* **504**, 423-426.

Holland HD (1978) *The Chemistry of the Atmosphere and Oceans,* John Wiley & Sons, New York.

Holland HD (1984) *The Chemical Evolution of the Atmosphere and Oceans,* Princeton Univ. Press, Princeton.

Holland HD (2006) The oxygenation of the atmosphere and oceans. *Phil. Trans. R. Soc. B,* **361**, 903-915.
Holser WT, Maynard JB, Cruikshank KM (1989) Modelling the natural cycle of sulphur through Phanerozoic time. In: *Evolution of the Global Biogeochemical Sulphur Cycle* (eds Brimblecombe P, Lein AY). John Wiley & Sons Ltd, New York, pp. 21-56.
Husson JM, Peters SE (2017) Atmospheric oxygenation driven by unsteady growth of the continental sedimentary reservoir. *Earth Planet. Sci. Lett.,* **460**, 68-75.
Jørgensen BB (1982) Mineralization of organic matter in the sea bed−the role of sulphate reduction. *Nature,* **296**, 643.
Jørgensen BB, Kasten S (2006) Sulfur cycling and methane oxidation. pp. 271-310.
Jones C, Nomosatryo S, Crowe SA, Bjerrum CJ, Canfield DE (2015) Iron oxides, divalent cations, silica, and the early earth phosphorus crisis. *Geology*.
Kagoshima T, Sano Y, Takahata N, Maruoka T, Fischer TP, Hattori K (2015) Sulphur geodynamic cycle. *Sci Rep,* **5**, 8330.
Kah LC, Lyons TW, Frank TD (2004) Low marine sulphate and protracted oxygenation of the Proterozoic biosphere. *Nature,* **431**, 834-838.
Kanzaki Y, Murakami T (2016) Estimates of atmospheric O_2 in the Paleoproterozoic from paleosols. *Geochim. Cosmochim. Acta,* **174**, 263-290.
Karl D, Michaels A, Bergman B, Capone D, Carpenter E, Letelier R, Lipschultz F, Paerl H, Sigman D, Stal L (2002) Dinitrogen fixation in the world's oceans. In: *The Nitrogen Cycle at Regional to Global Scales* (eds Boyer EW, Howarth RW). Springer Netherlands, Dordrecht, pp. 47-98.
Kharecha P, Kasting J, Siefert J (2005) A coupled atmosphere–ecosystem model of the early Archean Earth. *Geobiology,* **3**, 53-76.
Kump LR (1989) Chemical stability of the atmosphere and ocean. *Palaeogeogr. Palaeoclimatol. Palaeoecol.,* **75**, 123-136.
Kump LR, Arthur MA (1999) Interpreting carbon-isotope excursions: carbonates and organic matter. *Chem. Geol.,* **161**, 181-198.
Lasaga AC (1989) A new approach to isotopic modeling of the variation of atmospheric oxygen through the Phanerozoic. *Am. J. Sci.,* **289**, 411-435.
Lasaga AC, Ohmoto H (2002) The oxygen geochemical cycle: dynamics and stability. *Geochim. Cosmochim. Acta,* **66**, 361-381.
Laws EA, Falkowski PG, Smith WO, Ducklow H, Mccarthy JJ (2000) Temperature effects on export production in the open ocean. *Glob. Biogeochem. Cycles,* **14**, 1231-1246.
Lenton TM, Daines SJ (2017) Biogeochemical Transformations in the History of the Ocean. *Ann. Rev. Mar. Sci.,* **9**, 31-58.
Lin S, Morse JW (1991) Sulfate reduction and iron sulfide mineral formation in Gulf of Mexico anoxic sediments. *Am. J. Sci.,* **291**, 55-89.
Liss PS, Slater PG (1974) Flux of Gases across the Air-Sea Interface. *Nature,* **247**, 181-184.
Luo G, Ono S, Huang J, Algeo TJ, Li C, Zhou L, Robinson A, Lyons TW, Xie S (2015) Decline in oceanic sulfate levels during the early Mesoproterozoic. *Precambrian Res.,* **258**, 36-47.
Luo YW, Doney SC, Anderson LA, Benavides M, Berman-Frank I, Bode A, Bonnet S, Boström KH, Böttjer D, Capone DG, Carpenter EJ, Chen YL, Church MJ, Dore JE, Falcón LI, Fernández A, Foster RA, Furuya K, Gómez F, Gundersen K, Hynes AM, Karl DM, Kitajima S, Langlois RJ, Laroche J, Letelier RM, Marañón E, Mcgillicuddy Jr DJ, Moisander PH, Moore CM, Mouriño-Carballido B, Mulholland MR, Needoba JA, Orcutt KM, Poulton AJ, Rahav E, Raimbault P, Rees AP, Riemann L, Shiozaki T, Subramaniam A, Tyrrell T, Turk-Kubo KA, Varela M, Villareal TA, Webb EA, White AE, Wu J, Zehr JP (2012) Database of diazotrophs in global ocean: abundance, biomass and nitrogen fixation rates. *Earth Syst. Sci. Data,* **4**, 47-73.
Lyons TW, Gill BC (2010) Ancient Sulfur Cycling and Oxygenation of the Early Biosphere. *Elements,* **6**, 93-99.
Lyons TW, Reinhard CT, Planavsky NJ (2014) The rise of oxygen in Earth/'s early ocean and atmosphere. *Nature,* **506**, 307-315.
Maier-Reimer E (1993) Geochemical cycles in an ocean general circulation model. Preindustrial tracer distributions. *Glob. Biogeochem. Cycles,* **7**, 645-677.
Markovic S, Paytan A, Wortmann UG (2015) Pleistocene sediment offloading and the global sulfur cycle. *Biogeosciences,* **12**, 3043-3060.
Middelburg JJ, Soetaert K, Herman PMJ, Heip CHR (1996) Denitrification in marine sediments: A model study. *Glob. Biogeochem. Cycles,* **10**, 661-673.
Millero FJ, Plese T, Fernandez M (1988) THE DISSOCIATION OF HYDROGEN-SULFIDE IN SEAWATER. *Limnology and Oceanography,* **33**, 269-274.
Muller-Karger FE, Varela R, Thunell R, Luerssen R, Hu C, Walsh JJ (2005) The importance of continental margins in the global carbon cycle. *Geophys. Res. Lett.,* **32**.

Olson SL, Reinhard CT, Lyons TW (2016) Limited role for methane in the mid-Proterozoic greenhouse. *Proc. Natl Acad. Sci. USA,* **113**, 11447-11452.
Oschlies A, Schulz KG, Riebesell U, Schmittner A (2008) Simulated 21st century's increase in oceanic suboxia by CO2-enhanced biotic carbon export. *Glob. Biogeochem. Cycles,* **22**, n/a-n/a.
Ozaki K, Tajika E (2013) Biogeochemical effects of atmospheric oxygen concentration, phosphorus weathering, and sea-level stand on oceanic redox chemistry: Implications for greenhouse climates. *Earth Planet. Sci. Lett.,* **373**, 129-139.
Ozaki K, Tajima S, Tajika E (2011) Conditions required for oceanic anoxia/euxinia: Constraints from a one-dimensional ocean biogeochemical cycle model. *Earth Planet. Sci. Lett.,* **304**, 270-279.
Pallud C, Van Cappellen P (2006) Kinetics of microbial sulfate reduction in estuarine sediments. *Geochim. Cosmochim. Acta,* **70**, 1148-1162.
Pavlov AA, Kasting JF (2002) Mass-Independent Fractionation of Sulfur Isotopes in Archean Sediments: Strong Evidence for an Anoxic Archean Atmosphere. *Astrobiology,* **2**, 27-41.
Planavsky NJ, Bekker A, Hofmann A, Owens JD, Lyons TW (2012) Sulfur record of rising and falling marine oxygen and sulfate levels during the Lomagundi event. *Proc. Natl Acad. Sci. USA,* **109**, 18300-18305.
Planavsky NJ, Cole DB, Reinhard CT, Diamond C, Love GD, Luo G, Zhang S, Konhauser KO, Lyons TW (2016) No evidence for high atmospheric oxygen levels 1,400 million years ago. *Proc. Natl Acad. Sci. USA,* **113**, E2550-E2551.
Planavsky NJ, Reinhard CT, Wang X, Thomson D, Mcgoldrick P, Rainbird RH, Johnson T, Fischer WW, Lyons TW (2014) Low Mid-Proterozoic atmospheric oxygen levels and the delayed rise of animals. *Science,* **346**, 635-638.
Raiswell R, Canfield DE (2012) The Iron Biogeochemical Cycle Past and Present. *Geochemical Perspectives,* **1**, 1-2.
Reinhard CT, Planavsky NJ, Gill BC, Ozaki K, Robbins LJ, Lyons TW, Fischer WW, Wang C, Cole DB, Konhauser KO (2017) Evolution of the global phosphorus cycle. *Nature,* **541**, 386-389.
Romaniello SJ, Derry LA (2010) An intermediate-complexity model for simulating marine biogeochemistry in deep time: Validation against the modern global ocean. *Geochem. Geophys. Geosyst.,* **11**, n/a-n/a.
Ruttenberg KC (1993) Reassessment of the oceanic residence time of phosphorus. *Chem. Geol.,* **107**, 405-409.
Ruttenberg KC (2003) 8.13 - The Global Phosphorus Cycle A2 - Holland, Heinrich D. In: *Treatise on Geochemistry* (ed Turekian KK). Pergamon, Oxford, pp. 585-643.
Rye R, Holland HD (1998) Paleosols and the evolution of atmospheric oxygen; a critical review. *Am. J. Sci.,* **298**, 621-672.
Sarmiento JL, Gruber N (2006) *Ocean biogeochemical dynamics,* Princeton University Press.
Schlesinger WH, Bernhardt ES (2013) Chapter 13 - The Global Cycles of Sulfur and Mercury. In: *Biogeochemistry (Third Edition)*. Academic Press, Boston, pp. 469-486.
Scott C, Wing BA, Bekker A, Planavsky NJ, Medvedev P, Bates SM, Yun M, Lyons TW (2014) Pyrite multiple-sulfur isotope evidence for rapid expansion and contraction of the early Paleoproterozoic seawater sulfate reservoir. *Earth Planet. Sci. Lett.,* **389**, 95-104.
Shaffer G, Malskær Olsen S, Pepke Pedersen JO (2008) Presentation, calibration and validation of the low-order, DCESS Earth System Model (Version 1). *Geosci. Model Dev.,* **1**, 17-51.
Sleep NH (2005) Dioxygen over geological time. In: *Metal ions in biological systems* (eds Sigel A, Sigel H, Sigel RKO). Taylor & Francis Group, Boca Raton, pp. 49-73.
Steefel CI, Macquarrie KTB (1996) Approaches to modeling of reactive transport in porous media. *Reviews in Mineralogy and Geochemistry,* **34**, 85-129.
Stueken EE, Catling DC, Buick R (2012) Contributions to late Archaean sulphur cycling by life on land. *Nat. Geosci.,* **5**, 722-725.
Tang D, Shi X, Wang X, Jiang G (2016) Extremely low oxygen concentration in mid-Proterozoic shallow seawaters. *Precambrian Res.,* **276**, 145-157.
Tarhan LG, Droser ML, Planavsky NJ, Johnston DT (2015) Protracted development of bioturbation through the early Palaeozoic Era. *Nat. Geosci.,* **8**, 865.
Tarpgaard IH, Røy H, Jørgensen BB (2011) Concurrent low- and high-affinity sulfate reduction kinetics in marine sediment. *Geochim. Cosmochim. Acta,* **75**, 2997-3010.
Tostevin R, Turchyn AV, Farquhar J, Johnston DT, Eldridge DL, Bishop JKB, Mcilvin M (2014) Multiple sulfur isotope constraints on the modern sulfur cycle. *Earth Planet. Sci. Lett.,* **396**, 14-21.
Tromp TK, Van Cappellen P, Key RM (1995) A global model for the early diagenesis of organic carbon and organic phosphorus in marine sediments. *Geochim. Cosmochim. Acta,* **59**, 1259-1284.
Turchyn AV, Schrag DP (2004) Oxygen Isotope Constraints on the Sulfur Cycle over the Past 10 Million Years. *Science,* **303**, 2004-2007.
Turchyn AV, Schrag DP (2006) Cenozoic evolution of the sulfur cycle: Insight from oxygen isotopes in marine sulfate. *Earth Planet. Sci. Lett.,* **241**, 763-779.
Walker JCG, Brimblecombe P (1985) Iron and sulfur in the pre-biologic ocean. *Precambrian Res.,* **28**, 205-222.

Wallmann K (2003) Feedbacks between oceanic redox states and marine productivity: A model perspective focused on benthic phosphorus cycling. *Glob. Biogeochem. Cycles*, **17**, n/a-n/a.

Wallmann K (2010) Phosphorus imbalance in the global ocean? *Glob. Biogeochem. Cycles*, **24**, n/a-n/a.

Wallmann K, Pinero E, Burwicz E, Haeckel M, Hensen C, Dale A, Ruepke L (2012) The Global Inventory of Methane Hydrate in Marine Sediments: A Theoretical Approach. *Energies*, **5**, 2449.

Westrich JT, Berner RA (1984) The role of sedimentary organic matter in bacterial sulfate reduction: The G model tested1. *Limnology and Oceanography*, **29**, 236-249.

Williamson MA, Rimstidt JD (1994) The kinetics and electrochemical rate-determining step of aqueous pyrite oxidation. *Geochim. Cosmochim. Acta*, **58**, 5443-5454.

Wortmann UG, Paytan A (2012) Rapid Variability of Seawater Chemistry Over the Past 130 Million Years. *Science*, **337**, 334-336.

Yamanaka Y, Tajika E (1996) The role of the vertical fluxes of particulate organic matter and calcite in the oceanic carbon cycle: Studies using an ocean biogeochemical general circulation model. *Glob. Biogeochem. Cycles*, **10**, 361-382.

Yao W, Millero F (1995) The chemistry of the anoxic waters in the Framvaren Fjord, Norway. *Aquatic Geochemistry*, **1**, 53-88.

Yaroshevsky AA (2006) Abundances of chemical elements in the Earth's crust. *Geochem. Int.*, **44**, 48-55.

Yokota K, Kanzaki Y, Murakami T (2013) Weathering model for the quantification of atmospheric oxygen evolution during the Paleoproterozoic. *Geochim. Cosmochim. Acta*, **117**, 332-347.

Zhang S, Wang X, Wang H, Bjerrum CJ, Hammarlund EU, Dahl TW, Canfield DE (2016) Reply to Planavsky et al.: Strong evidence for high atmospheric oxygen levels 1,400 million years ago. *Proc. Natl Acad. Sci. USA*, **113**, E2552-E2553.